

THE COYOTE UNIVERSE II: COSMOLOGICAL MODELS AND PRECISION EMULATION OF THE NONLINEAR MATTER POWER SPECTRUM

KATRIN HEITMANN¹, DAVID HIGDON², MARTIN WHITE³, SALMAN HABIB⁴, BRIAN J. WILLIAMS², EARL LAWRENCE², AND CHRISTIAN WAGNER⁵

¹ ISR-1, ISR Division, Los Alamos National Laboratory, Los Alamos, NM 87545

² CCS-6, CCS Division, Los Alamos National Laboratory, Los Alamos, NM 87545

³ Departments of Physics and Astronomy, University of California, Berkeley, CA 94720

⁴ T-2, Theoretical Division, Los Alamos National Laboratory, Los Alamos, NM 87545

⁵ Astrophysikalisches Institut Potsdam (AIP), An der Sternwarte 16, D-14482 Potsdam

Draft version May 28, 2018

ABSTRACT

The power spectrum of density fluctuations is a foundational source of cosmological information. Precision cosmological probes targeted primarily at investigations of dark energy require accurate theoretical determinations of the power spectrum in the nonlinear regime. To exploit the observational power of future cosmological surveys, accuracy demands on the theory are at the one percent level or better. Numerical simulations are currently the only way to produce sufficiently error-controlled predictions for the power spectrum. The very high computational cost of (precision) N -body simulations is a major obstacle to obtaining predictions in the nonlinear regime, while scanning over cosmological parameters. Near-future observations, however, are likely to provide a meaningful constraint only on constant dark energy equation of state, ‘ w CDM’, cosmologies. In this paper we demonstrate that a limited set of only 37 cosmological models – the ‘‘Coyote Universe’’ suite – can be used to predict the nonlinear matter power spectrum to one percent over a prior parameter range set by current cosmic microwave background observations. This paper is the second in a series of three, with the final aim to provide a high-accuracy prediction scheme for the nonlinear matter power spectrum for w CDM cosmologies.

Subject headings: methods: statistical — cosmology: large-scale structure of the universe

1. INTRODUCTION

Although the discovery of cosmic acceleration by Riess et al. (1998) and Perlmutter et al. (1999) is already a decade in the past, our understanding of the nature of the underlying driver of the acceleration, ‘‘dark energy’’, has made little progress. One reason for this is that the dark energy equation of state parameter w is consistent with a cosmological constant ($w = -1$) at roughly 10% accuracy, with no constraints on any possible time dependence. In order to advance further in terms of distinguishing different models of dark energy from each other and dark energy itself from other possible causes of acceleration (such as a possible break-down of general relativity on very large scales) observational errors must be brought down significantly. The current target is to achieve another order of magnitude improvement for several dark energy probes – probes that measure not only the expansion history of the Universe but also the growth of cosmological structure – down to the level of a percent.

To date, the five most promising lines of investigation are: (i) Supernovae Type Ia, to measure the expansion history of the Universe, (ii) clusters of galaxies, to measure the expansion history and growth of structure, (iii) baryon acoustic oscillations, to measure the expansion history, (iv) weak lensing, to measure the expansion history and the growth of structure and (v) redshift distortions to measure the growth of structure. The last three probes, baryon acoustic oscillations, weak lensing and redshift space distortions, rely the most strongly on precise predictions of the nonlinear matter power spectrum. Numerical simulations are essential for carrying out this task, not only for the power spectrum itself, but also to build the underlying skeleton of cosmological structure from which object catalogs can be constructed. The resulting ‘mock catalogs’ have many uses: to design and test observational strategies, to understand system-

atic errors therein, and to confront theoretical predictions with observations.

In the case of baryon acoustic oscillations, measurements are carried out on very large scales, where the nonlinear effects are small. Therefore, higher order perturbation theory might offer an alternative path to obtaining precise predictions for the nonlinear matter power spectrum (see, e.g., Crocce & Scoccimarro 2006; Matsubara 2008; Pietroni 2008; Carlson et al. 2009; Padmanabhan 2009 and references therein), and provide a useful foil for the numerical results. Weak lensing measurements go down to much smaller spatial scales, out to wavenumbers $k \sim 1 - 10 h\text{Mpc}^{-1}$ (and even larger wavenumbers in the future). On these smaller length scales, perturbative techniques fail, and one must rely on numerical simulations to obtain the required level of accuracy: at least as accurate as the observations, and to be optimal, substantially more accurate. As shown by, e.g. Huterer & Takada (2003), to avoid biasing of cosmological parameter estimations a wide-field weak lensing survey such as the SNAP¹ design requires 1% accurate power spectrum predictions, and a survey such as the Large Synoptic Survey Telescope (LSST²) requires predictions at the 0.5% accuracy level.

These requirements pose two major challenges: First, one must show that simulations capturing the essential physics have reached the desired level of accuracy. For baryon acoustic oscillations, it is expected that gravity-only N -body simulations, augmented by halo occupancy modeling, are sufficient for the task. In the case of weak lensing, this assumption holds for scales out to $k \sim 1 h\text{Mpc}^{-1}$. In the first paper of this series (Heitmann et al. 2008) we have established that, up to these scales, the nonlinear matter power spectrum can be determined

¹<http://snap.lbl.gov>

²<http://www.lsst.org>

at sub-percent accuracy by gravity-only N -body simulations. At smaller scales, baryonic physics becomes important at the few to ten percent level and has to be taken into account (White 2004; Zhan & Knox 2004; Jing et al. 2006; Rudd et al. 2008; Guillet, Teyssier & Colombi 2009), a task which has to be tackled accurately in the near future, perhaps by a suitable combination of simulations and observations.

After overcoming the first challenge, the next task in constraining cosmological parameters, is to cover a range of different cosmologies. Markov Chain Monte Carlo (MCMC) methods, commonly used for parameter determination, rely on results from model evaluations numbering in the tens of thousands to hundreds of thousands. Since an accurate N -body simulation on the scales of interest mentioned above costs of the order of $\sim 20,000$ CPU-hours, it is not feasible to run such simulations for each model. (Running $\sim 20,000$ N -body simulations with the required resolution on a contemporary 2048 processor cluster would take 20 years!) Taking into account the fact that adding gasdynamics and feedback effects substantially increases both the computational load and the number of parameters to be varied, it is clear that a brute force approach to the problem has to be avoided. What we need is a generalized interpolation method capable of yielding very accurate predictions for the nonlinear matter power spectrum from a restricted number of simulations. In the following, we will refer to such a prediction scheme as an emulator. The emulator will be tasked with replacing brute force N -body simulations for the nonlinear matter power spectrum over a pre-defined set of cosmological parameters, with specified ranges for the chosen parameters.

In the cosmic microwave background (CMB) community several different paths have been suggested to provide such an emulator for the CMB temperature anisotropy power spectrum. These include purely analytic fits (Tegmark & Zaldarriaga 2000; Jimenez et al. 2004) and combinations of analytic and semi-analytic fits (Kaplinghat et al. 2002). More recently, neural network methods and machine learning techniques have been successfully used to generate very accurate temperature anisotropy power spectra (Fendt & Wandelt 2007a; Auld et al. 2007; Fendt & Wandelt 2007b; Auld et al. 2008). These methods are based on a large number of training sets, up to several tens of thousands. (For an alternative approach requiring many fewer simulations, see Habib et al. 2007.) While this does not constitute a problem for anisotropy power spectra – given the speeds at which numerical codes such as CAMB and CMBFast can be run – the approach is not feasible for determining the matter power spectrum, which requires large-scale supercomputer simulations.

As in the case for the temperature anisotropy power spectrum, several attempts have been made to avoid costly simulations by finding good approximations for the nonlinear matter power spectrum. These range from more or less analytic derivations (e.g., Hamilton et al. 1991; Peacock & Dodds 1994) to semi-analytic fits calibrated more specifically against simulation results (e.g., Peacock & Dodds 1996; Smith et al. 2003). Unfortunately, the accuracy of these approximations is inadequate, at best reaching the 5-10% level (see, e.g., Heitmann et al. 2008 for a recent comparison of precision simulations with HALOFIT, a fitting scheme due to Smith et al. 2003). Thus, an order of magnitude improvement is needed to address the accuracy requirements discussed above.

Accurate emulation is needed for many observational quantities in cosmology, power spectra being one important ex-

ample. To address this need, we have recently introduced the ‘‘Cosmic Calibration Framework’’ (Heitmann et al. 2006; Habib et al. 2007; Schneider et al. 2008) combining sophisticated simulation designs with Gaussian process (GP) modeling to create very accurate emulators from a restricted set of simulations. The term ‘simulation design’ refers to the specific choice of parameter settings at which to carry out the simulations. One of the main reasons why the Cosmic Calibration Framework provides very accurate results from only a small number of training sets is the optimization of the simulation design strategy to work well with the chosen interpolation scheme, the Gaussian process in this particular case. Another useful aspect of the methodology is that it contains an error prediction scheme, so that one can verify the consistency of the obtained results.

In this paper we will explain and demonstrate the emulation capability of the Cosmic Calibration Framework. With only a small number of simulations, an emulator for the nonlinear matter power spectrum can be constructed, matching the simulation results at the level of 1% accuracy. We focus on the regime of spatial wavenumber $k \lesssim 1 h\text{Mpc}^{-1}$ and a redshift range between $z = 0$ and $z = 1$, covering the current space of interest for weak lensing measurements. Such an emulator will eliminate a major source of bias in determining cosmological parameters from weak lensing data. In order to design, construct, and test an emulator, it is useful to carry out the process first on a proxy for the expensive numerical simulations; the proxy need not be very accurate but should reflect the overall behavior of the detailed simulations; we employ HALOFIT in this role.

This paper is the second in a series of three communications. In the first, we have demonstrated that it is possible to obtain nonlinear matter power spectra at sub-percent level accuracy out to $k \simeq 1 h\text{Mpc}^{-1}$ from simulations, having derived and presented a set of requirements for such simulations. The third paper of the series will present results from the complete simulation suite based on the cosmologies presented in the current paper, as well as the public release of a precision power spectrum emulator. The simulation suite is named the ‘‘Coyote Universe’’ after the computer cluster it has been carried out on.

The paper is organized as follows. In Section 2 we describe in detail the Cosmic Calibration Framework with special emphasis on building a nonlinear matter power spectrum emulator from a restricted set of simulations. We explain the design strategy for generating the training sets and discuss the emulation step, demonstrating the emulator accuracy. Next we provide a sensitivity analysis showing how the power spectrum varies – in a scale-dependent manner – as the cosmological parameters are changed. We present our conclusions in Section 3.

2. THE COSMIC CALIBRATION FRAMEWORK

The Cosmic Calibration Framework (Heitmann et al. 2006; Habib et al. 2007; Schneider et al. 2008) consists of four interlocking steps: (i) the simulation design, which determines at what parameter settings to generate the training sets, (ii) generation of the emulator which replaces the simulator as a predictor of results away from the points that were used to generate the training set, (iii) the uncertainty and sensitivity analysis associated with the emulator, and (iv) the calibration against data via MCMC methods to determine parameter constraints.

In the following we discuss steps (i) - (iii) in detail, with special emphasis on generating an accurate emulator for the nonlinear matter power spectrum.

2.1. Sampling the Model Space

As discussed in the Introduction, one of the major challenges in building an accurate emulator for the nonlinear matter power spectrum is the very high cost of individual N -body simulations combined with the high dimensionality of the parameter space (which may include cosmological, physical, and numerical modeling parameters). To sample the model space, the number of parameters to be varied must be specified, as well as the range of variation for each parameter. For now, we will assume that some combination of observational knowledge and cosmological and astrophysical modeling is sufficient to decide on conservative choices for sampling the model space. (We will return to this question later, in Section 2.1.2.)

Following this decision, the next step is to find a method for sampling the model space and interpolating the results therefrom, satisfying given accuracy criteria, and using only a manageable number of simulation design points. In several applications, space-filling Latin hypercube (LH) designs (details below) have proven to be well suited for the GP model-based approach (Sacks et al. 1989a; Currin et al. 1991) to solving the interpolation problem. The Cosmic Calibration Framework uses this methodology; the associated validation examples can be found in Heitmann et al. (2006) and Habib et al. (2007).

In the following, we first discuss the statistical aspects of sampling model space followed by the observational aspects, i.e., the parameters to be varied and the corresponding choices for the range of variation. The parameter choices and prior ranges from observations used here rely on the most recent CMB observations from WMAP-5 (Komatsu et al. 2008).

2.1.1. Statistical Sampling Methods

Our first aim is to find a distribution of the parameter settings – the simulation design – which provides optimal coverage (in a sense to be defined below) of the parameter space, using only a limited number of sampling points. (In the statistics literature, it is customary to use normalized units in which all parameters range over the interval $[0, 1]$ and we will follow this usage for the most part.) If the actual behavior of the observable as a function of the parameters is considered to be unknown, then it is sensible to start with a strategy that attempts to uniformly sample the space (space-filling design). An extreme version of this is a simple, regular hypercubic grid. The problem with using a grid-based interpolation method is the high dimensionality of the space. Suppose we wish to vary 5 cosmological parameters and sample each parameter only three times – at near-maximum, near-minimum, and in the middle of each parameter range. Already, this would require $3^5 = 243$ simulations – not a small number – and lead to poor coverage of the parameter space. Such a design with only 3 levels (three sampling points per parameter) would also only allow for estimating a quadratic model. If we want to go to a higher level, the number of runs will explode – if we wish to keep the complete grid. If on the other hand, we try to reduce the number of runs by using only a fraction of the grid, aliasing becomes a potential problem.

The opposite extreme of pure random sampling suffers from clustering of sample points and occurrence of large voids in the sampling region when the number of sample points is limited. Stratified sampling techniques combine the idea of a regular grid and random sampling by using strata that (equally) sub-divide the sample space, with random sampling employed within each strata. A final important point is that the computed observable may depend on some sub-combination of input vari-

ables (factor sparsity), in which case we would like to have uniform coverage across the projection of the full space onto the relevant factors. Not all uniform sampling schemes possess this property.

The GP model interpolation scheme used here does not require a simple grid design. Simulation designs well-suited for GP model emulators are LH-based designs, a type of stratified sampling scheme. Latin hypercube sampling generalizes the Latin square for two variables, where only one sampling point can exist in each row and each column. A Latin hypercube sample – in arbitrary dimensions – consists of points stratified in each (axis-oriented) projection. More formally, an LH design is an $n \times m$ matrix in which each column is a unique random permutation of $\{1, \dots, n\}$. The use of LH designs in applications where the aim is to predict the outcome of some quantity at untried parameter settings from a restricted set of simulations was first proposed by McKay et al. (1979). As discussed in more detail below, like many other interpolators, GP models rely on local information for their interpolation strategy. Therefore, the simulation design must provide good coverage over the whole parameter space. Space-filling LH designs and their variants provide an effective means for achieving this.

Very often LH designs are combined with other design strategies such as orthogonal array (OA)-based designs or are optimized in other ways, e.g., by symmetrizing them (more details below). By intelligently melding design strategies, different attributes of the individual sampling strategies can be combined to lead to improved designs, and shortcomings of specific designs can be eliminated. As a last step, optimization schemes are often applied to spread out the points evenly in a projected space. One such optimization scheme is based on minimizing the maximal distance between points in the parameter space, which will lead to more even coverage. We provide some details about different optimization schemes in Appendix A. For a discussion of different design approaches and their specific advantages see, e.g., Santner et al. (2003).

We now briefly discuss two design strategies well suited to cosmological applications in which the number of parameters is much less than the number of simulations that can be performed. These are optimal OA-LH design strategies and optimal symmetric LH design strategies. The former has been used in previous work in cosmology (Heitmann et al. 2006; Habib et al. 2007), while the latter will be used in this paper to construct the design for the Coyote Universe. For illustration purposes, we will use a very simple, three-dimensional case example with three parameters, $\theta_1, \theta_2, \theta_3$ and nine sampling points.

In order to create an OA-LH design, the strategy proceeds in two steps: (i) construction of the orthogonal array and (ii) the following construction of the orthogonal-array based Latin hypercube. We discuss these two steps in turn following closely the description by Tang (1993) and Leary et al. (2003).

OA Designs

An orthogonal array distributes runs uniformly in certain projections of the full parameter space. The mathematical definition is as follows: An n by m matrix \mathbf{A} with entries from a set $1, 2, \dots, s$ is called an orthogonal array of strength r , size n , with m constraints, and s levels, if each $n \times r$ submatrix of \mathbf{A} contains all possible $1 \times r$ rows with the same frequency λ . Here λ is termed the index of the array, and $n = \lambda s^r$. The array is denoted $\text{OA}(n, m, s, r)$ (Tang 1993).

For our application, n denotes the number of simulation runs to be performed and m specifies the number of parameters to be varied (these can be cosmological parameters as well as numerical input parameters). These choices fix the number of dimensions in the parameter hypercube. The parameter s defines the levels of stratification for each column in the matrix \mathbf{A} . In order to sample the parameter space well in a uniform manner, it is often not enough to sample it well globally. For example, if two or more parameters interact strongly with each other, it is clearly desirable to have a good space-filling design in the subspace of these parameters. In other words, if one projects the design down onto, e.g. two dimensions, such a projection should have space-filling properties in those dimensions as well. The parameter r , the strength of OA designs, indicates the projections for which the LH design based on that OA are guaranteed to be space-filling. For example, if $r = 3$, then all 1, 2 and 3 dimensional projections will be space-filling. Obviously, r cannot be larger than m , the number of parameters varied.

The strength, r , is usually restricted to two or three for several reasons: (i) Fewer and fewer OA designs with appropriate run sizes are known as the strength increases (more on this below). (ii) In most applications, only a small number of parameters influence the response significantly. Statisticians call this the “20-80 rule” – 20% of the parameters being responsible for 80% of the outcome variation. Therefore, the aim is to capture the action of these relevant parameters. Furthermore, outcome variation is often dominated by a small number of single parameter and two-factor interaction effects, which are adequately covered by OA-LH designs based on $r = 2$ or 3. (iii) The number of simulations often has to be kept small, therefore r cannot be chosen too large, since the number of simulations n is connected to r via $n = \lambda s^r$. As is the case for r , the stratification parameter s is also restricted by the number of runs one can possibly perform. It is very often set to $s = 2$ which then requires the number of runs to be a power of two. The frequency λ with which a permutation repeats, is kept small as well. To create a design, the strategy is to fix strength first, and try to find an OA design that has approximately the right number of runs and at least as many parameters as one needs. If such a design cannot be found, then the strength is reduced by one and the process repeated. Usually, this strategy is started with OA designs of strength 3, though many more designs of strength 2 exist. It is rarely possible to find a strength four or higher design with few enough runs.

The above discussion points to a shortcoming of orthogonal arrays: the number of simulation runs cannot be picked arbitrarily (e.g., choosing $s = 2$ forces a power of two for the number

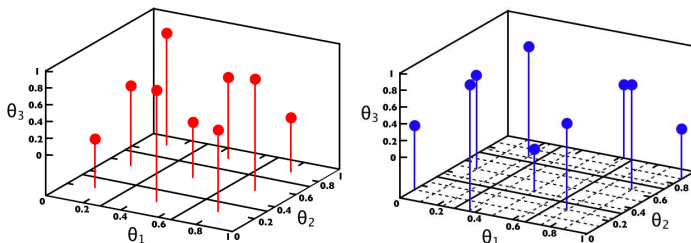


FIG. 1.— Left panel: an orthogonal array (OA) based design for 3 parameters, θ_1 , θ_2 , θ_3 and nine sampling points. Right panel: the OA based design perturbed in such a way that the one-dimensional projection onto any parameter leads to an equally spaced distribution of sample points. The projection onto any two dimensions leads to a space filling design.

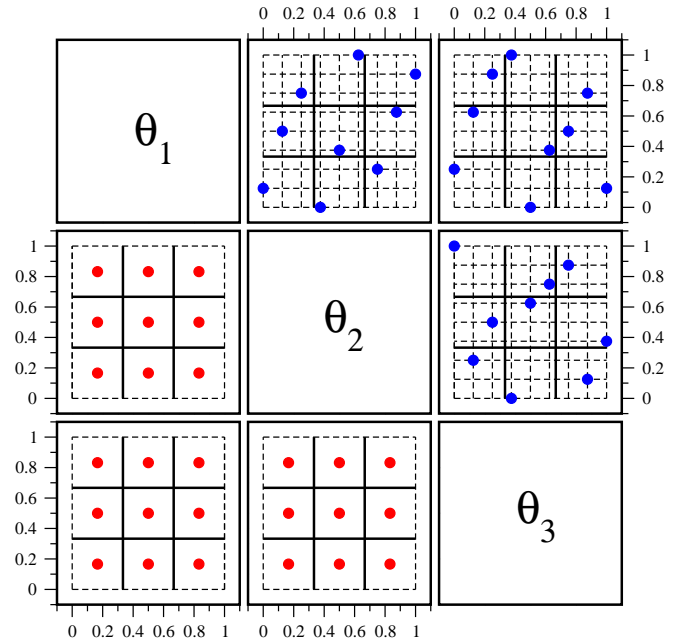


FIG. 2.— Projections of the design shown in Figure 1 onto two dimensions. The lower triangle shows the projection of the OA design, the upper triangle of the OA-LH design. Note that when projected onto one dimension, the OA-LH design leads to an even coverage and no points lie on top of each other.

of runs). The other difficulty with orthogonal arrays is that they are not easy to construct.³

Some of the preceding discussion can be best understood by studying a specific case. Consider an example with nine sampling points ($n = 9$) and three parameters ($m = 3$). If we require $r > 1$ for the strength of the design, then the relation $n = \lambda s^r$ leads automatically to an OA design with $s = 3$ levels, strength $r = 2$, $\lambda = 1$; an $\text{OA}(9, 3, 3, 2)$ design. We require that if we project our design down onto any two-dimensional direction, the parameter space be well covered. The left panel in Figure 1 shows a possible realization of an OA with our example specifications. The lower triangle in Figure 2 shows the three possible two-dimensional projections of this design. This specific design is of course not a unique solution. In matrix form it reads:

$$\begin{pmatrix} \theta_1 & \theta_2 & \theta_3 \\ 1 & 1 & 1 \\ 2 & 1 & 3 \\ 3 & 1 & 2 \\ 1 & 2 & 2 \\ 2 & 2 & 1 \\ 3 & 2 & 3 \\ 1 & 3 & 3 \\ 2 & 3 & 2 \\ 3 & 3 & 1 \end{pmatrix} \xrightarrow{[0,1]} \begin{pmatrix} 0.166 & 0.166 & 0.166 \\ 0.5 & 0.166 & 0.832 \\ 0.832 & 0.166 & 0.5 \\ 0.166 & 0.5 & 0.5 \\ 0.5 & 0.5 & 0.166 \\ 0.832 & 0.5 & 0.832 \\ 0.166 & 0.832 & 0.832 \\ 0.5 & 0.832 & 0.5 \\ 0.832 & 0.832 & 0.166 \end{pmatrix}. \quad (1)$$

From this 9×3 matrix we can now verify that each of the three 9×2 sub-matrices indeed contain all possible 1×2 rows with the same frequency $\lambda = 1$. On the right hand side of Eq. (1) we have simply rescaled the design points into the normalized $[0,1]$ space which is shown in Figures 1 and 2.

³A detailed description of OA designs and how to construct them is given in Hedayat et al. (1999). A library containing a large number of OAs can be found at: <http://www.research.att.com/~njas/oadir/index.html>. A collection of C routines to generate OA designs can be found at: <http://lib.stat.cmu.edu/designs/oa.c>.

OA-LH Designs

In order to further improve parameter space coverage, the next step – Latin hypercube sampling – perturbs the positions of each sampling point from \mathbf{A} via the following prescription: for each column of \mathbf{A} , the λs^{r-1} positions with entry k are replaced by a permutation of $(k = 1, \dots, s)$

$$(k-1)\lambda s^{r-1} + 1, (k-1)\lambda s^{r-1} + 2, \dots, (k-1)\lambda s^{r-1} + \lambda s^{r-1} = k\lambda s^{r-1}. \quad (2)$$

This means, in our example, that the entries for $k = 1$ will be replaced by 1,2,3, the entries for $k = 2$ will be replaced by 4,5,6, and the entries for $k = 3$ by 7,8,9. The Latin hypercube algorithm demands that in every column every entry appears only once. This ensures that each one dimensional projection is evenly covered with points and no run is replicated in the resulting design. The right panel in Figure 1 shows a possible realization of this in three dimensions, derived from perturbing the orthogonal array in the left panel. The upper right triangle in Figure 2 shows the two-dimensional projection of this design. The solid lines show the division for the orthogonal array while the dashed lines show the additional sub-division. Note that each sample point lies on a unique horizontal and vertical dashed line – if the sample points are projected down onto any one direction, the one-dimensional space would be evenly covered. In matrix form, our OA-LH design is as follows:

$$\begin{pmatrix} 1 & 2 & 3 \\ 4 & 1 & 9 \\ 7 & 3 & 5 \\ 2 & 5 & 6 \\ 5 & 4 & 1 \\ 8 & 6 & 7 \\ 3 & 7 & 8 \\ 6 & 9 & 4 \\ 9 & 8 & 2 \end{pmatrix} \xleftrightarrow{[0,1]} \begin{pmatrix} 0 & 0.125 & 0.25 \\ 0.375 & 0 & 1 \\ 0.75 & 0.25 & 0.5 \\ 0.125 & 0.5 & 0.625 \\ 0.5 & 0.375 & 0 \\ 0.875 & 0.625 & 0.75 \\ 0.25 & 0.75 & 0.875 \\ 0.625 & 1 & 0.375 \\ 1 & 0.875 & 0.125 \end{pmatrix}. \quad (3)$$

Note that we have replaced the entries in a random fashion and created this design “by hand” – convincing ourselves “by eye” that we have good coverage in 2-D projection. Leary et al. (2003) suggest an optimal strategy to ensure even better coverage of the parameter space. These optimization strategies are often used for the projected parameter space. In order for the points to be spread out, one has to determine the ‘closeness’ between them. This can be defined as the smallest distance between any two points. A design that maximizes this measure is said to be a maximin distance design. (For more details, see Santner et al. 2003 and Appendix A.) The designs in Heitmann et al. (2006) and Habib et al. (2007) combine the OA-LH based design with a maximin distance design in each two-dimensional projection. Other optimization methods rest on an entropy criterion based on the minimization of $-\log|R|$, where R is the covariance matrix of the design (Shewry & Wynn 1987), or minimization of the Integrated Mean Squared Error (Sacks et al. 1989b).

Our example shows just one way to realize an OA-LH design. It can be implemented straightforwardly and leads to the desired coverage of the parameter space. After the design has been determined in the $[0, 1]$ parameter space, it then can be easily translated into the physical parameter space of interest. At this point, when projected down to one dimension, the equidistant coverage in each dimension of the parameter space in one dimension is of course lost. However, since our transformation is linear, we do not lose the uniformity of the projections.

Therefore it is still true that no two sample points will fall on top of each other in projection.

SLH designs

As mentioned above, the major restriction of OA-LH based designs is that they cannot be set up for an arbitrary number of simulation runs. This is a specific point of concern, if one can only run a very restricted number of simulations. In addition, the set-up of an OA-LH design can be nontrivial. Very often, one has to rely on OA libraries which are restricted in their parameters and also not always easily available. An alternative space-filling design strategy presented by Li & Ye (2000), offers a compromise between the computing effort and the design optimality – the optimal symmetric Latin hypercube designs. Following their definition, an LH design is called a symmetric LH (SLH) design if it has the following property: For any row i of an LH design, there exists another row in the design which is the i th row’s reflection through the center. For example, in an $n \times m$ Latin hypercube with levels from 1 to n , if (a_1, a_2, \dots, a_m) is one of the rows, the vector $(n+1-a_1, n+1-a_2, \dots, n+1-a_m)$ should be another row in the design. The symmetry imposes a space-filling requirement on the designs considered up front, which carries through to all projections. An example for an SLH design is given by:

$$\begin{pmatrix} 1 & 2 & 3 \\ 8 & 7 & 6 \\ 4 & 1 & 2 \\ 5 & 8 & 7 \\ 7 & 3 & 5 \\ 2 & 6 & 4 \\ 3 & 4 & 1 \\ 6 & 5 & 8 \end{pmatrix}. \quad (4)$$

In this design, rows 1/2, 3/4, 5/6, and 7/8 are symmetric pairs. As before, we do not attempt to optimize the resulting design (though the design we use later in the paper is optimized, see below). The two-dimensional projection of the design given in Eq. (4) is shown in Figure 3.

Li & Ye (2000) provide an excellent discussion of optimal SLH designs, including a description of possible algorithmic implementations and comparison with traditional optimal LH designs. As an example, they show that the computational effort to find an optimal LH design by starting with an SLH design reduces roughly by a factor of ten for a 25×4 design on a workstation. As before, the SLH design is usually optimized in the last step, often with respect to a distance based criterion which spreads out the points in two-dimensional projections. Two standard search algorithms for an optimal SLH design are the columnwise-pairwise (CP) algorithm by Ye (1998) and

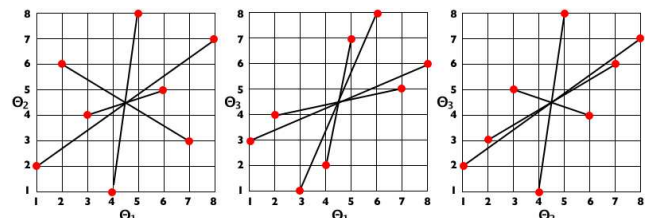


FIG. 3.— Two-dimensional projections of the SLH design given in Eq. (4). The symmetric design points are connected to show the reflection through the center.

the simulated annealing (SA) algorithm by Morris & Mitchell (1995). (More details about the SA and CP algorithms are given in Appendices A.2 and A.3, respectively). Simply put, these algorithms are based on columnwise exchanges of entries which will keep the symmetry properties (since the corresponding symmetric pairs are always switched at the same time). They are iterative procedures, which will stop after a certain pre-set optimization criterion is fulfilled or the process is interrupted by time limitations. Very often, several designs are produced at the same time and the most optimal kept in the end. The SA and CP algorithms can also be used to optimize OA-LH designs. If the OA skeleton is symmetric, then one can require the optimal OA-LH design to be symmetric as well.

In the following, we will use an LH design optimized via a distance criterion. The design will encompass 37 simulation runs and five cosmological parameters. In detail, 20 optimizations with CP and 20 with SA were carried out, and the best was chosen in the end where the quality was measured by a distance criterion. For CP, 10 of the designs had a symmetry requirement and the other 10 did not. For SA, 10 of the designs had a symmetry requirement and were optimized with a local optimization criterion, and the other 10 did not have a symmetry requirement and were optimized with a more global optimization criterion. The best design from all of these came from one of the optimizations using SA, a global optimization criterion, and no symmetry requirement.

2.1.2. Observational Considerations

The choice of number of active parameters depends on the available data as well as on the chosen modeling approach. We

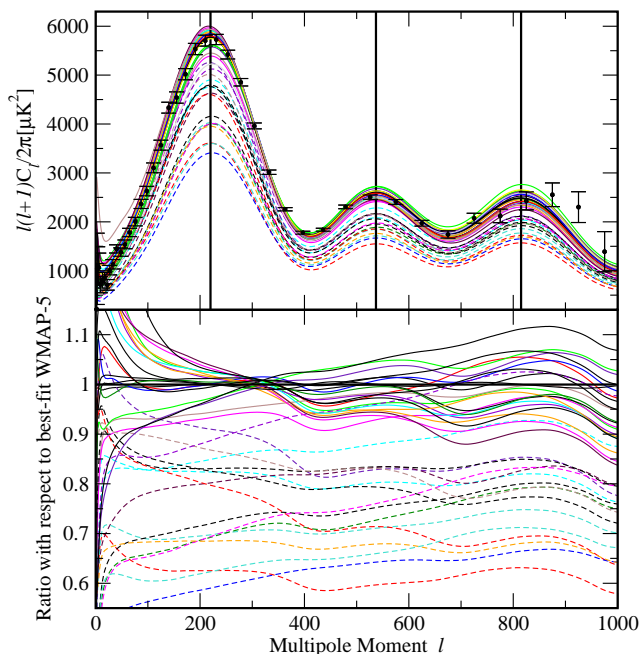


FIG. 4.— Best-fit TT power spectra for each model in Table 1 using the WMAP-5 results. The only parameter which has been optimized by minimizing χ^2 is the optical depth τ . The upper panel shows the resulting power spectra, the black points with error bars show WMAP-5 data points, and the thick black line the best-fit WMAP-5 model. The lower panel shows the residuals for each model with respect to the best-fit model. Some of our models are undernormalized, the best-fit τ being smaller than 0.01 which would lead to a reionization redshift of $z < 2$ and χ^2 for these models is larger than 3000 (the χ^2 for the best-fit WMAP-5 model is at roughly 2650). We fixed τ for those models at $\tau = 0.01$ and show them with dashed lines.

do not insist on a formal methodology to make this choice, but instead present practical and conservative arguments to justify our decisions. We take as our basic 5 parameters $\omega_m \equiv \Omega_m h^2$, $\omega_b \equiv \Omega_b h^2$, n_s , w , and σ_8 where Ω_m contains the contributions from the dark matter and the baryons. We restrict ourselves to power-law models (no running of the spectral index), to spatially flat models without massive neutrinos and to dark energy models with constant equation of state. A sixth parameter, the redshift or time, simply requires us to dump data from each run at multiple epochs. The choice of these parameters is dictated by the physics underlying the matter power spectrum, and the combinations of cosmological parameters that are well constrained by existing (primarily CMB) data (see also White & Vale 2004).

The effect of massive neutrinos can be roughly approximated by decreasing Ω_m (Brandbyge et al. 2008). We do not expect any realistic dark energy model to have a constant equation of state, but we wanted to begin with the most restrictive parameter space in order to validate our methods. The next generation of experiments will pose at best weak constraints on any time variation of w , and in this sense our constant w can be thought of as an appropriate average of $w(z)$. Using growth matching techniques (White & Vale 2004; Linder & White 2005; Francis et al. 2007) one can map the power spectrum from a complex $w(z)$ onto one with a constant w with reasonable accuracy.

The normalization is another area where choices need to be made. Historically the amplitude of the power spectrum was set by σ_8 , the amplitude of the *linear theory* matter power spectrum smoothed with a top-hat on scales of $8h^{-1}\text{Mpc}$

$$\sigma_8^2 \equiv \int \frac{dk}{k} \Delta_{\text{lin}}^2(k) \left[\frac{3j_1(kR)}{kR} \right]^2 \Bigg|_{R=8h^{-1}\text{Mpc}}, \quad (5)$$

with the linear power spectrum being defined as

$$\Delta_{\text{lin}}^2(k) \equiv \frac{k^3 P_{\text{lin}}(k)}{2\pi^2}. \quad (6)$$

This scale and normalization were chosen because the fluctuations of counts of L_* galaxies in cells of this size is close to unity. With the advent of the COBE data it became common to quote the normalization at horizon scales, e.g. Bunn & White (1997). As CMB data improved, the pivot point was shifted to smaller scales, closer to the middle of the range over which the spectrum is probed and where the normalization is best determined. In order to make closer connection with the initial fluctuations, the amplitude not of the matter power spectrum but of the curvature or potential fluctuations has been adopted. These differ mostly by factors of growth and Ω_m . Anticipating future advances, $k_p = 0.002\text{Mpc}^{-1}$ was selected for the most recent CMB analysis by Komatsu et al. (2008) and the rms curvature fluctuation on this scale is now most commonly used as a normalization. With present CMB data the biggest uncertainties in the normalization are the near degeneracy with the optical depth, τ , and the uncertain growth of perturbations at low redshift due to the unknown equation of state of the dark energy, e.g. White (2006).

For our purposes, however, a normalization tied to the present day matter power spectrum and close to the nonlinear scale has many advantages. Rather than introduce yet another convention, we therefore choose to use σ_8 as our normalization parameter. Of course, since all of the parameters of the models are specified one can compute any other parameter for our models. As an example, we have evaluated for each of the models

TABLE 1
PARAMETERS FOR 38 MODELS

| # | ω_m | ω_b | n_s | $-w$ | σ_8 | # | ω_m | ω_b | n_s | $-w$ | σ_8 |
|----|------------|------------|--------|-------|------------|----|------------|------------|--------|-------|------------|
| 0 | 0.1296 | 0.0224 | 0.9700 | 1.000 | 0.8000 | 19 | 0.1279 | 0.0232 | 0.8629 | 1.184 | 0.6159 |
| 1 | 0.1539 | 0.0231 | 0.9468 | 0.816 | 0.8161 | 20 | 0.1290 | 0.0220 | 1.0242 | 0.797 | 0.7972 |
| 2 | 0.1460 | 0.0227 | 0.8952 | 0.758 | 0.8548 | 21 | 0.1335 | 0.0221 | 1.0371 | 1.165 | 0.6563 |
| 3 | 0.1324 | 0.0235 | 0.9984 | 0.874 | 0.8484 | 22 | 0.1505 | 0.0225 | 1.0500 | 1.107 | 0.7678 |
| 4 | 0.1381 | 0.0227 | 0.9339 | 1.087 | 0.7000 | 23 | 0.1211 | 0.0220 | 0.9016 | 1.261 | 0.6664 |
| 5 | 0.1358 | 0.0216 | 0.9726 | 1.242 | 0.8226 | 24 | 0.1302 | 0.0226 | 0.9532 | 1.300 | 0.6644 |
| 6 | 0.1516 | 0.0229 | 0.9145 | 1.223 | 0.6705 | 25 | 0.1494 | 0.0217 | 1.0113 | 0.719 | 0.7398 |
| 7 | 0.1268 | 0.0223 | 0.9210 | 0.700 | 0.7474 | 26 | 0.1347 | 0.0232 | 0.9081 | 0.952 | 0.7995 |
| 8 | 0.1448 | 0.0223 | 0.9855 | 1.203 | 0.8090 | 27 | 0.1369 | 0.0224 | 0.8500 | 0.836 | 0.7111 |
| 9 | 0.1392 | 0.0234 | 0.9790 | 0.739 | 0.6692 | 28 | 0.1527 | 0.0222 | 0.8694 | 0.932 | 0.8068 |
| 10 | 0.1403 | 0.0218 | 0.8565 | 0.990 | 0.7556 | 29 | 0.1256 | 0.0228 | 1.0435 | 0.913 | 0.7087 |
| 11 | 0.1437 | 0.0234 | 0.8823 | 1.126 | 0.7276 | 30 | 0.1234 | 0.0230 | 0.8758 | 0.777 | 0.6739 |
| 12 | 0.1223 | 0.0225 | 1.0048 | 0.971 | 0.6271 | 31 | 0.1550 | 0.0219 | 0.9919 | 1.068 | 0.7041 |
| 13 | 0.1482 | 0.0221 | 0.9597 | 0.855 | 0.6508 | 32 | 0.1200 | 0.0229 | 0.9661 | 1.048 | 0.7556 |
| 14 | 0.1471 | 0.0233 | 1.0306 | 1.010 | 0.7075 | 33 | 0.1399 | 0.0225 | 1.0407 | 1.147 | 0.8645 |
| 15 | 0.1415 | 0.0230 | 1.0177 | 1.281 | 0.7692 | 34 | 0.1497 | 0.0227 | 0.9239 | 1.000 | 0.8734 |
| 16 | 0.1245 | 0.0218 | 0.9403 | 1.145 | 0.7437 | 35 | 0.1485 | 0.0221 | 0.9604 | 0.853 | 0.8822 |
| 17 | 0.1426 | 0.0215 | 0.9274 | 0.893 | 0.6865 | 36 | 0.1216 | 0.0233 | 0.9387 | 0.706 | 0.8911 |
| 18 | 0.1313 | 0.0216 | 0.8887 | 1.029 | 0.6440 | 37 | 0.1495 | 0.0228 | 1.0233 | 1.294 | 0.9000 |

Note. — The five basic parameters for the 37 models that specify the simulation design and model 0 which we use as an independent check. See text for definitions.

given in Table 1 the best-fit value for τ using the likelihood code provided by the WMAP-5 team. The resulting TT power spectra are shown in Figure 4 as well as their ratios with respect to the best-fit WMAP-5 model. Some of our models are undernormalized and the resulting τ is smaller than 0.01 leading to reionization redshifts of $z < 2$. This undernormalization however is not a concern: we chose the models to cover the parameter space well overall and not to provide fits close to the concordance cosmology. We provide the best-fit values for τ in Table 2.

From the WMAP 5-year data, in combination with BAO, we

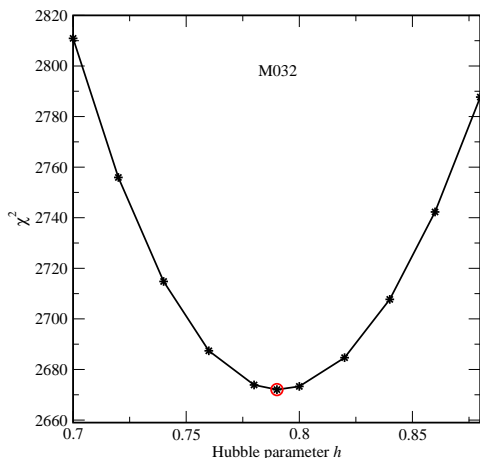


FIG. 5.— Sweep through h for model 32. The red circle marks the estimate for the Hubble parameter from assuming perfect knowledge of ℓ_A , in excellent agreement with the result from the WMAP-5 likelihood for the best-fit value of h for this model.

have⁴

$$\begin{aligned} \omega_m &= 0.1347 \pm 0.0040 \quad (3\%), \\ \omega_b &= 0.0227 \pm 0.0006 \quad (3\%), \\ n_s &= 0.9610 \pm 0.0140 \quad (2\%). \end{aligned} \quad (7)$$

Current data restrict a constant equation of state for the dark energy to $w = -1$ with roughly 10% accuracy (for very recent results from supernovae see, e.g., Kowalski et al. 2008; for weak lensing see, e.g., Kilbinger et al. 2008; and for the latest constraints from clusters of galaxies, see Vikhlinin et al. 2008). Recent determinations put the normalization in the range 0.7–0.9 with still rather large uncertainties (see, e.g., Vikhlinin et al. 2008 for constraints from clusters, Voevodkin & Vikhlinin 2004 for a low estimate from clusters, Tegmark et al. 2007 for constraints from combined CMB and large scale structure data, and Evrard et al. 2008 for an extended discussion of recent results). Considering all these constraints and their uncertainties, we choose our sample space boundaries to be

$$\begin{aligned} 0.120 &< \omega_m < 0.155, \\ 0.0215 &< \omega_b < 0.0235, \\ 0.85 &< n_s < 1.05, \\ -1.30 &< w < -0.70, \\ 0.61 &< \sigma_8 < 0.9, \end{aligned} \quad (8)$$

as shown in Table 1.

In order to solve for the full set of cosmological parameters we impose the CMB constraint that $\ell_A \equiv \pi d_{ls}/r_s = 302.4$, where d_{ls} is the distance to the last scattering surface and r_s is the sound horizon. Observationally this is known to 0.3%, and models which significantly violate this equality are poor fits to the CMB data (see Figure 5). Unfortunately the sound horizon, like the epoch of last scattering, can be defined in a number of different ways which differ subtly. Specifically we use the fit to the redshift of last scattering of Eq. (23) of Hu & White (1997)

⁴See <http://lambda.gsfc.nasa.gov/>

TABLE 2
DERIVED PARAMETERS FOR 38 MODELS

| # | Ω_m | Ω_{de} | h | d_{ls} | $\tau(\chi^2)$ | # | Ω_m | Ω_{de} | h | d_{ls} | $\tau(\chi^2)$ |
|----|------------|---------------|--------|----------|----------------|----|------------|---------------|--------|----------|----------------|
| 0 | 0.2500 | 0.7500 | 0.7200 | 14.24 | 0.1 | 19 | 0.1940 | 0.8060 | 0.8120 | 14.24 | < 0.01 (7712) |
| 1 | 0.4307 | 0.5693 | 0.5977 | 13.59 | 0.064 | 20 | 0.3109 | 0.6891 | 0.6442 | 14.27 | 0.15 |
| 2 | 0.4095 | 0.5905 | 0.5970 | 13.80 | 0.205 | 21 | 0.2312 | 0.7688 | 0.7601 | 14.14 | < 0.01 (21579) |
| 3 | 0.2895 | 0.7105 | 0.6763 | 14.10 | 0.19 | 22 | 0.3317 | 0.6683 | 0.6736 | 13.70 | < 0.01 (11139) |
| 4 | 0.2660 | 0.7340 | 0.7204 | 13.99 | < 0.01 (5569) | 23 | 0.1602 | 0.8398 | 0.8694 | 14.48 | < 0.01 (4478) |
| 5 | 0.2309 | 0.7691 | 0.7669 | 14.11 | < 0.01 (2756) | 24 | 0.1854 | 0.8146 | 0.8380 | 14.21 | < 0.01 (13138) |
| 6 | 0.3059 | 0.6941 | 0.7040 | 13.66 | < 0.01 (19318) | 25 | 0.4558 | 0.5442 | 0.5724 | 13.76 | < 0.01 (3033) |
| 7 | 0.3310 | 0.6690 | 0.6189 | 14.31 | 0.225 | 26 | 0.2804 | 0.7196 | 0.6931 | 14.05 | 0.14 |
| 8 | 0.2780 | 0.7220 | 0.7218 | 13.84 | < 0.01 (4320) | 27 | 0.3357 | 0.6643 | 0.6387 | 14.04 | 0.08 |
| 9 | 0.3707 | 0.6293 | 0.6127 | 13.93 | < 0.015 (2845) | 28 | 0.3988 | 0.6012 | 0.6189 | 13.66 | 0.06 |
| 10 | 0.3131 | 0.6869 | 0.6695 | 13.98 | 0.05 | 29 | 0.2516 | 0.7484 | 0.7067 | 14.32 | < 0.01 (2809) |
| 11 | 0.2790 | 0.7210 | 0.7177 | 13.82 | < 0.01 (3928) | 30 | 0.2810 | 0.7190 | 0.6626 | 14.37 | 0.155 |
| 12 | 0.2235 | 0.7765 | 0.7396 | 14.43 | < 0.01 (5901) | 31 | 0.3791 | 0.6209 | 0.6394 | 13.62 | < 0.01 (17774) |
| 13 | 0.3974 | 0.6026 | 0.6107 | 13.77 | < 0.01 (11549) | 32 | 0.1922 | 0.8078 | 0.7901 | 14.47 | 0.115 |
| 14 | 0.3289 | 0.6711 | 0.6688 | 13.74 | < 0.01 (11803) | 33 | 0.2634 | 0.7366 | 0.7286 | 13.96 | < 0.01 (2829) |
| 15 | 0.2363 | 0.7637 | 0.7737 | 13.89 | < 0.01 (9905) | 34 | 0.3532 | 0.6468 | 0.6510 | 13.71 | 0.1 |
| 16 | 0.1981 | 0.8019 | 0.7929 | 14.40 | 0.025 | 35 | 0.3990 | 0.6010 | 0.6100 | 13.77 | 0.135 |
| 17 | 0.3586 | 0.6414 | 0.6305 | 13.94 | < 0.01 (5012) | 36 | 0.2949 | 0.7051 | 0.6421 | 14.41 | 0.455 |
| 18 | 0.2578 | 0.7422 | 0.7136 | 14.22 | < 0.01 (5641) | 37 | 0.2796 | 0.7204 | 0.7313 | 13.71 | < 0.01 (2971) |

Note. — The derived parameters, obtained from the basic parameters listed in Table 1 by applying the constraint on ℓ_A . Only for model 0 is the Hubble parameter picked by hand. The distance to last scattering is in Gpc, all other parameters are dimensionless. See text for details.

and use Eq. (B6) of Hu & Sugiyama (1995) for the sound horizon. With these choices we find models with ω_m and ω_b in the range preferred by WMAP do indeed provide good fits to the WMAP data. This is demonstrated for model 32 in Figure 5.

The procedure is then as follows. For every specified ω_m and ω_b we compute r_s and hence the required d_{ls} to fit the ℓ_A constraint. We adjust h , at fixed spatial curvature, w , and ω_m , until the model reproduces the required d_{ls} . Knowing h and ω_m then gives us Ω_m and hence Ω_{de} , as shown in Table 2.

Finally, we generated a model ‘0’ which has parameters close to the current best fit from CMB and large-scale structure (e.g., Komatsu et al. 2008). This model has $\Omega_m = 0.25$, $\Omega_{de} = 0.75$, $\omega_b = 0.0224$, $n_s = 0.97$, $h = 0.72$, and $\sigma_8 = 0.8$ and can be used as an independent check of the interpolation in the range of most interest.

2.1.3. The Resulting Design

Based on the above considerations, we can now generate a space-filling design for the five parameters of interest. We restrict ourselves to 37 cosmologies and will show in the remainder of the paper that this number is indeed sufficient to generate an accurate emulator. For model 0 we pick a standard LCDM model for which we chose the Hubble parameter by hand (although $h = 0.72$ is very close to the result we would obtain if we would derive it from d_{ls}). The resulting cosmological models are listed in Table 1 where we give the values for the basic parameters. In Table 2 we give in addition a few derived parameters: Ω_m , Ω_{de} (recall that flatness is assumed), h as derived from our constraint on ℓ_A , d_{ls} , and τ .

The two-dimensional projections of the design are shown in Figure 6. The upper part of the triangle shows the five input parameters in red, demonstrating a good sampling of the parameter space. The blue points show projections of three of the derived parameters, Ω_m , h , and d_{ls} .

The key statistical observable discussed in this paper is the density fluctuation power spectrum $P(k)$, the (ensemble-averaged) Fourier transform of the two-point density correlation function. In dimensionless form, the power spectrum can be written as

$$\Delta^2(k) \equiv \frac{k^3 P(k)}{2\pi^2}, \quad (9)$$

equivalent to the linear power spectrum in Eq. (5). Figure 7 shows the resulting dimensionless HALOFIT power spectra for the 38 cosmological models at $z = 1$ (left panel) and at $z = 0$

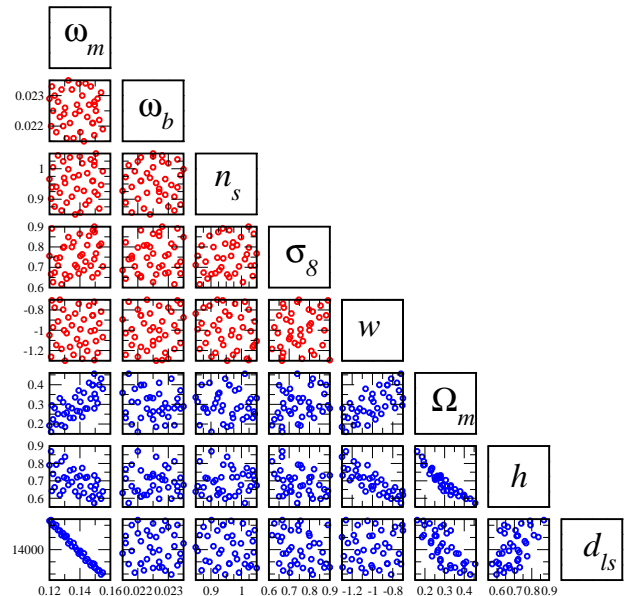


FIG. 6. — Final simulation design: The five parameters under consideration are shown in red, projected onto two dimensions. The blue points show three derived parameters: Ω_m , h , and d_{ls} .

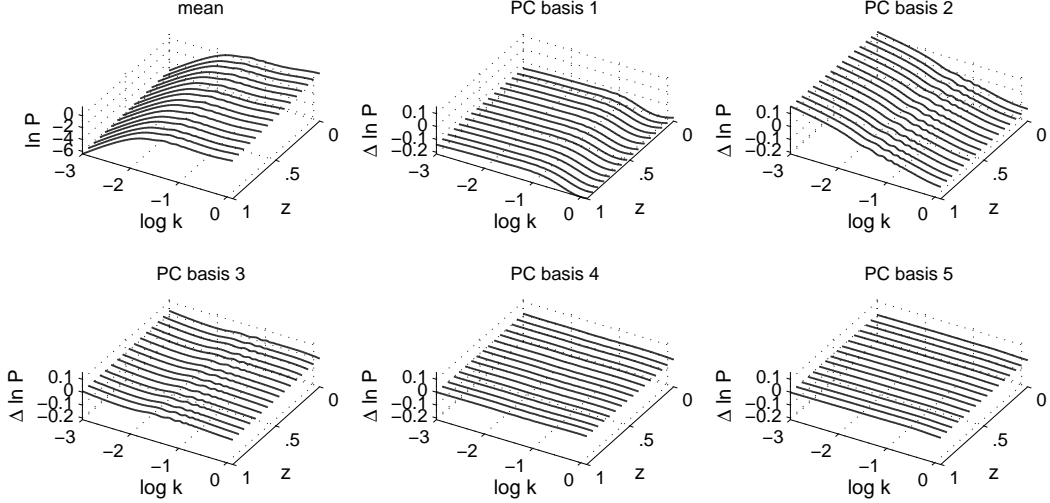


FIG. 8.— Mean (upper left corner) and five principal component (PC) bases derived from the output from the 38 HALOFIT power spectra. The third axis shows the time evolution of the mean and the five principal components between redshift $z = 1$ and $z = 0$. While the first two principal component bases show significant variation, the fourth and fifth are already almost flat, indicating that the inclusion of higher principal components would not improve the quality of the emulator and the underlying GP model.

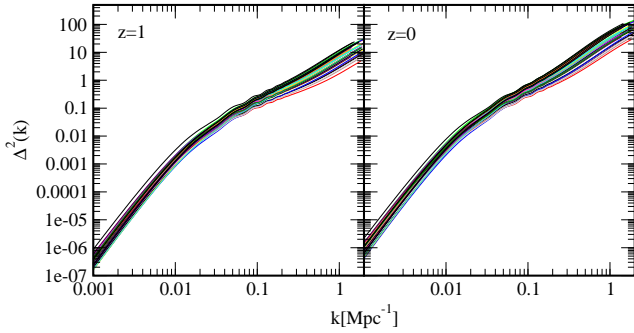


FIG. 7.— Dimensionless power spectra as given by HALOFIT for the 38 cosmologies specified in Table 1 at $z = 1$ (left panel) and $z = 0$ (right panel).

(right panel)⁵. Overall, the parameter space is well covered by these 38 models, the coverage being sufficient to accommodate upcoming weak lensing survey measurements.

2.2. Emulation

After specifying the design, the next task is to construct the emulator for predicting the nonlinear matter power spectrum within the parameter priors specified in the design. For an in-depth mathematical description of building such an emulator in the cosmological context we refer the reader to Habib et al. (2007) and Schneider et al. (2008). Here we explain the major ideas behind the process and show explicitly the emulator performance for our 37 model design. As discussed in the Introduction, we use HALOFIT as a proxy for the full numerical simulations as a convenient foil to demonstrate and to test the overall procedure.

Before constructing the emulator, it is useful to find the best-possible representation of the power spectrum. The major aim is to find a representation that preserves the smoothness of the power spectrum but at the same time enhances important features, such as the baryon acoustic oscillations. It turns out to be

⁵Note that we are using Mpc^{-1} units for k in this paper, not $h\text{Mpc}^{-1}$ as in Heitmann et al. (2008). We omit the h since the underlying physics determines the shape of the power spectrum better in Mpc^{-1} units than $h\text{Mpc}^{-1}$ units (e.g. White 2006).

more convenient to model the power spectrum as

$$\mathcal{P}(k, z; \theta) = \ln \left\{ \frac{\Delta^2(k, z)}{2\pi k^{3/2}} \right\} \quad (10)$$

than to work with $\Delta^2(k, z; \theta)$ directly (the connection between $\Delta^2(k)$ and $\mathcal{P}(k)$ is given in Eq. (9), θ denotes the cosmological parameters varied). This transformation reduces the total dynamic range as well as enhances the baryon acoustic oscillation features in the power spectrum.

In order to construct the emulator, we represent the scaled power spectrum $\mathcal{P}(k, z; \theta)$ using an $n_{\mathcal{P}}$ -dimensional basis:

$$\mathcal{P}(k, z; \theta) = \mu_{\mathcal{P}}(k, z) + \sum_{i=1}^{n_{\mathcal{P}}} \phi_i(k, z) w_i(\theta) + \epsilon, \quad \theta \in [0, 1]^{n_{\theta}}, \quad (11)$$

where the ϕ_i are the basis functions and the w_i are the corresponding weights. We have stored each power spectrum at 200 k values between $-3 \leq \log_{10} k \leq 0.12$ and 100 z values between $0 \leq z \leq 1$. Therefore, $\mathcal{P}(k, z; \theta)$ represents the power spectra, over a 200×100 grid of k and z values. Over this grid, the values $\mathcal{P}(k, z; \theta)$ are determined by the five cosmological parameters denoted by θ . The dimensionality $n_{\mathcal{P}}$ refers to the number of orthogonal basis vectors $\{\phi_1(k, z), \dots, \phi_{n_{\mathcal{P}}}(k, z)\}$. As we will show later, $n_{\mathcal{P}} = 5$ turns out to be an adequate choice for the present application. The parameter n_{θ} is the dimensionality of our parameter space – with 5 cosmological parameters we have $n_{\theta} = 5$ (that $n_{\mathcal{P}} = n_{\theta}$ here is a coincidence). As mentioned earlier, it is convenient to map the parameter ranges into $[0, 1]$ via a linear transformation. The last term in Eq. (11), ϵ , is the error term. Our main tasks in building the emulator are now:

- Find a suitable set of orthogonal basis vectors $\phi_i(k, z)$. In our case, a principal components basis turns out to be an efficient representation, but alternative representations may be employed. We found it convenient to construct the basis vectors in (k, z) space, though one could also build a separate basis for each redshift.
- Model the weights $w_i(\theta)$ as smooth functions of the underlying parameters, θ . Our choice of GP models is based on their success in representing functions

that change smoothly with parameter variation, e.g., the variation of the power spectrum as a function of cosmological parameters.

2.2.1. The Principal Component Basis

Before we determine the basis vectors to model the simulation output for the power spectrum $\mathcal{P}(k, z; \theta)$, we standardize the simulation power spectra in the following way. We first center the power spectra around their mean, given by $\mu_{\mathcal{P}}(k, z) = \frac{1}{37} \sum_{j=1}^{37} \mathcal{P}_j$. The resulting mean as a function of redshift z and wavenumber k is shown in the upper left corner of Figure 8. (Remember that we divide $\Delta^2(k, z)$ by $2\pi k^3/2$ leading to the flattening of the power spectrum at high k .) After having centered the simulations around the mean, we scale the output by a single value for each k and z so that its variance is one.

The next step is the principal component analysis (PCA) to determine the orthogonal basis vectors $\phi_i(k, z)$ for modeling the simulation output for the power spectra following Eq. (11). To carry out this step, we write the standardized power spectra as an $n_{kz} \times m$ matrix, where $n_{kz} = 20000$ is the number of support points for each power spectrum over the 200×100 k - z grid, and $m = 37$ is the number of cosmological models⁶. The $n_{kz} \times m$ matrix reads:

$$Y_{\text{sims}} = [\mathcal{P}_1; \dots; \mathcal{P}_{37}]. \quad (12)$$

Following Habib et al. (2007), we apply a singular value decomposition to the simulation output matrix Y_{sims} giving

$$Y_{\text{sims}} = UDV^T, \quad (13)$$

where U is an $n_{kz} \times m$ orthogonal matrix, D is a diagonal $m \times m$ matrix holding the singular values, and V is an $m \times m$ orthonormal matrix. The PC basis matrix $\Phi_{\mathcal{P}}$ is now defined to be the first $n_{\mathcal{P}}$ columns of $[UD/\sqrt{m}]$ and the principal component weights are given by $W = [\sqrt{m}V]$. Here the i^{th} column of W (given by $w_i^* = (w_{i1}^*, \dots, w_{im}^*)$) holds the weights corresponding to the basis function $\phi_i(k, z)$ for the $m = 37$ simulations run at cosmologies $\theta_1^*, \dots, \theta_m^*$. The star indicates quantities derived from the m simulations.

In order to model the nonlinear matter power spectrum, we find that five principal components are sufficient to capture all information. Therefore we have $n_{\mathcal{P}} = 5$ and $\Phi_{\mathcal{P}} = [\phi_1; \phi_2; \phi_3; \phi_4; \phi_5]$. The resulting five PC bases are shown in Figure 8 as a function of z and k . The fourth and the fifth components are already very flat – increasing the dimensionality further would not improve the quality of the data representation.

2.2.2. Gaussian Process Modeling

The final step is to model the PC weight functions $w_i(\theta)$, $i = 1, \dots, n_{\mathcal{P}}$, in Eq. (11) conditioned on the known results from the 37 cosmological models. We will employ Gaussian process modeling for this task. Gaussian process modeling is a nonparametric regression approach particularly well suited for interpolation of smooth functions over a parameter space. As mentioned previously, GP models are local interpolators and work well with space-filling sampling techniques. The GP (also

⁶As mentioned above, we could also determine the orthogonal basis vectors separately for each z output. In this case, we would obtain 100 matrices of size 200×37 each. One could fit separate GP's for each z , but such a model will require 500 GPs, instead of 5. While we have not tried fitting separate GPs at each z , we expect the resulting emulator performance will be similar. Using basis elements over the (k, z) support results in a simpler model and much easier computations for parameter estimation and emulation.

called Gaussian random functions) is simply a generalization of the Gaussian probability distribution, extending the notion of a Gaussian distribution over scalar or vector random variables to function spaces. (For an excellent introduction to Gaussian processes, see Rasmussen & Williams 2006.) The Gaussian distribution is specified by a scalar mean μ or a mean vector and a covariance matrix – extending this to the GP leads to a specification of the GP by a mean function and a covariance function.

In order to build an emulator from a GP three steps have to be performed:

- **Specification of the Gaussian Process:** Define a GP model which is determined by its mean and covariance specification. A priori, realizations of functions produced from this model should cover a (specified) range of possibilities for the simulation response, here the PC weights $w_i(\theta)$.
- **Statistical Parameter Estimation:** The statistical parameters controlling the GP model are estimated from the known simulation outputs via either maximum likelihood or Bayesian methods, in order to obtain good predictive performance from the emulator.
- **The Conditional Process:** Once the statistical parameters have been estimated, the GP model is fully specified. Because of its Gaussian form, it can now be conditioned analytically to the simulation output: The conditional process produces random functions which are constrained to pass through the observed output and give predictions, with uncertainties, at untried θ values.

We now describe each of these steps for a single one of the $w_i(\theta)$'s; for simplicity we will ignore the subscript. From the SVD decomposition of the simulation output described in Section 2.2.1, we also have the observed weights obtained from the 37 simulations which are in the 37-vector w^* . The complete procedure to obtain the emulator for the power spectra is more involved, in part due to the higher dimensionality of the problem. The interested reader can find details on this procedure in Appendix B.

Specification of the Gaussian Process

The first step is to define the GP from which we can generate random function realizations $w(\theta)$. For a GP, any finite restriction of $w(\theta)$ has a multivariate Gaussian distribution. A priori, at any single θ , we take $w(\theta)$ to be mean-zero (although this is not necessary), with variance $\sigma^2 = \lambda_w^{-1}$. At two points θ and θ' the $w(\theta)$ and $w(\theta')$ are correlated:

$$\text{Corr}[w(\theta), w(\theta')] \equiv R(\theta, \theta'). \quad (14)$$

The correlation function R as defined above is critical to the GP approach. In addition to being positive definite, it typically has the following attributes: (i) for $\theta = \theta'$ it is unity, so that replicates are perfectly correlated; (ii) it is large when $\theta \simeq \theta'$, capturing the notion that two nearby points are highly correlated, (iii) it is small when θ is far away from θ' so that far separated points are essentially uncorrelated. A commonly used form for the correlation function is given by

$$R(\theta, \theta'; \vartheta) = \prod_{j=1}^{n_{\theta}} \exp(-\vartheta_j |\theta_j - \theta'_j|^{p_j}). \quad (15)$$

The corresponding GP covariance function is given by $\Sigma(\theta, \theta') = \sigma^2 R(\theta, \theta'; \vartheta)$. As previously, the dimension of the problem is denoted by n_θ . Large values of ϑ_j (analog to an inverse correlation length) allow for more complexity in the j^{th} component direction for the function we want to model. The value for p is typically set to be either one or two. The choice $p = 2$ yields very smooth realizations with infinitely many derivatives, while $p = 1$ leads to rougher realizations suited to modeling continuous but non-differentiable (stochastic) functions. Throughout this paper we will use $p = 2$.

Statistical Parameter Estimation

We treat the simulation output w^* , produced at the 37 input settings, as a partial realization of the prior GP model. Therefore, given the covariance parameters σ^2 and ϑ , w^* is a draw from a $m = 37$ -dimensional Gaussian distribution

$$p(w^* | \sigma^2, \vartheta_1, \dots, \vartheta_{n_\theta}) = (2\pi\sigma^2)^{-m/2} \det(R)^{-1/2} \exp\left\{-\frac{1}{2\sigma^2} w^{*T} R(\theta^*; \vartheta)^{-1} w^*\right\}. \quad (16)$$

Here $R(\theta^*; \vartheta)$ denotes the 37×37 correlation matrix obtained by applying Eqn. (15) to each pair of simulated cosmologies in θ^* .

Maximum likelihood estimates for σ^2 and ϑ can be obtained by finding the parameter values $(\hat{\sigma}^2, \hat{\vartheta})$ that maximize Eqn. (16) above. Conditional on knowing the correlation parameters ϑ , the likelihood is maximized for σ^2 at

$$\hat{\sigma}^2 = \frac{1}{m} w^{*T} R(\theta^*; \vartheta)^{-1} w^*. \quad (17)$$

Maximizing with respect to the components of ϑ must be done numerically. Once estimated, we can insert these values in Eqn. (16) and treat the GP specification as fully known.

An alternative is to use a Bayesian approach as detailed in Habib et al. (2007) or, more generally in Higdon et al. (2008), to find the optimal parameters of the GP. While such an approach requires additional prior specifications and computational effort, it does account for uncertainties in the covariance parameters and the resulting prediction. This can be important if the emulator is used along with physical observations to estimate cosmological parameters. The resulting emulator predictions are not very sensitive to either approach. The analysis presented in this paper follows the Bayesian approach detailed in the references above. Therefore, we obtain a posterior distribution for the covariance parameters, rather than a point estimate as in maximum likelihood. Figure B14 shows boxplots of the marginal posterior distribution for each of the correlation parameters. We provide details on this approach in Appendix B.

The Conditional Process

We can now fix σ^2 and ϑ at their estimated values, and treat them as known. The next step is to construct the conditional process for $w(\theta)$ given the output w^* of the 37 simulations. This new, conditional process is also a GP, but realizations of it are random functions that are constrained to interpolate the simulation output. For any input setting θ , the conditional process describes $w(\theta)$ with a normal distribution:

$$p(w(\theta) | w^*, \hat{\sigma}^2, \hat{\vartheta}) = (2\pi\hat{\sigma}_\theta^2)^{-m/2} \det(R)^{-1/2} \times \exp\left\{-\frac{1}{2\hat{\sigma}_\theta^2} (w(\theta) - \mu_\theta)^T R(w(\theta) - \mu_\theta)\right\}. \quad (18)$$

Here μ_θ and σ_θ^2 are determined by the parameters σ^2 , ϑ , by the simulation output w^* , and by the componentwise distances between the new prediction setting θ and design $\theta_1^*, \dots, \theta_{37}^*$. Specifically,

$$\begin{aligned} \mu_\theta &= r(\theta) R(\theta^*; \vartheta)^{-1} w^* \\ \sigma_\theta^2 &= \sigma^2 [1 - r(\theta) R(\theta^*; \vartheta)^{-1} r(\theta)'] \end{aligned}$$

where

$$r(\theta) = \{R(\theta, \theta_1^*; \vartheta), \dots, R(\theta, \theta_{37}^*; \vartheta)\}. \quad (19)$$

The emulator uses the conditional mean μ_θ as the estimate for $w(\theta)$. The prediction for the power spectrum $\mathcal{P}(k, z; \theta)$ can then be produced using Eqn. (11).

2.2.3. Emulator Performance

In order to evaluate the accuracy of the emulator we generate a second set of ten power spectra with HALOFIT within the prior parameter ranges for three redshifts, $z = 0, 0.5$, and 1. For this set we choose the input cosmologies randomly, but still insuring that the constraint on the Hubble parameter is satisfied. The ten additional cosmologies are listed in Table 3. We then predict the results for those cosmologies with the emulator scheme and compare them to the HALOFIT output, the ‘‘truth’’ in this case. The results for the residuals are shown in Figure 9.

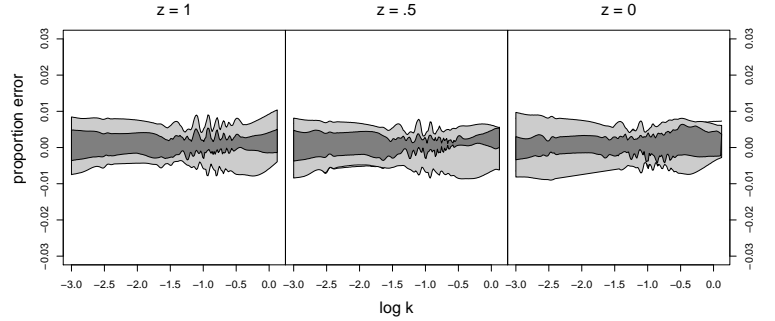


FIG. 9.— Emulator performance at three redshifts, $z = 1, 0.5$ and 0 (left to right). The emulator is tested on 10 additional HALOFIT runs within the parameter priors. The emulator error with respect to the HALOFIT results is shown. The central gray region contains the middle 50% of the residuals, the wider light gray region, the middle 90%. Errors are at the sub-percent level. We emphasize that we do not show the average of the residuals, which would artificially suppress the error, but rather represent the residuals by the two bands.

The middle 50% of the residuals (dark gray band) are accurate to 0.5% or better over the entire k -range and for all three

TABLE 3
PARAMETERS FOR 10 TEST MODELS

| ω_m | ω_b | n_s | $-w$ | σ_8 |
|------------|------------|--------|--------|------------|
| 0.1327 | 0.0220 | 0.8890 | 0.8406 | 0.7235 |
| 0.1524 | 0.0219 | 0.8792 | 0.9515 | 0.7926 |
| 0.1542 | 0.0224 | 0.8533 | 1.1044 | 0.8630 |
| 0.1428 | 0.0235 | 1.0302 | 1.1359 | 0.8740 |
| 0.1372 | 0.0226 | 0.9474 | 0.7219 | 0.8877 |
| 0.1337 | 0.0228 | 0.9499 | 0.7392 | 0.7985 |
| 0.1386 | 0.0229 | 1.0260 | 0.8145 | 0.7870 |
| 0.1490 | 0.0228 | 0.9979 | 1.1144 | 0.8156 |
| 0.1250 | 0.0229 | 0.9031 | 0.7963 | 0.7916 |
| 0.1214 | 0.0228 | 1.0043 | 0.9418 | 0.7555 |

redshifts. All predictions have errors less than 1%. This result shows that a simulation set with as small a number as 37 cosmologies is sufficient to produce a power spectrum emulator accurate at 1%.

In Habib et al. (2007) several other convergence tests are discussed and demonstrated. These tests show that emulator performance can improve considerably – by an order of magnitude – if either the number of simulation training runs is increased or the parameter space under consideration is narrowed. In the present paper we follow the second strategy, restricting the priors as much as is sensible given the current and near-future observational situation.

2.3. Sensitivity Analysis

After the emulator has been built it can be used to explore the behavior of the power spectrum – within the parameter priors – in more detail than if one had access only to the results at the design points. Because this can be done quickly and in a straightforward manner, an obvious use of emulation is to carry out a sensitivity analysis, i.e. study the behavior of the power spectrum as the underlying cosmological input parameters are varied. It is also very useful to carry out a sensitivity analysis of quantities related to the GP modeling itself, such as the principal component weight functions and the correlation functions. Such an analysis is important to ensure that the GP model is robust and accurate and will lead, in addition, to more insight about the global importance of different cosmological parameters.

A first example of a sensitivity analysis is represented in Figure 10. Here we show variations of the power spectrum at three redshifts $z = 0$, $z = 0.5$, and $z = 1$. The reference power spectrum is that obtained with every parameter fixed at the midpoint of its prior range, i.e., in this case, for the cosmology $\omega_m = 0.1375$, $\omega_b = 0.02215$, $n_s = 0.95$, $w = -1$, $\sigma_8 = 0.758$. (This power spectrum is close to the mean of the 37 models from our design, but not the same.) Next, only one parameter is varied between its

maximum and minimum value while the other four parameters are fixed at their midpoints. In Figure 10 from left to right we vary ω_m , ω_b , n_s , σ_8 , and w , showing the difference between natural logarithms of these two power spectra. We note that the Hubble parameter is different for each power spectrum shown in the figure since it is separately optimized for each cosmology.

The results contain information about the scales at which the power spectrum is most sensitive to each parameter and about parameter degeneracies. For example, it is clear that the power spectrum is relatively insensitive to ω_b , within the allowed range, at any scale or redshift and it will therefore be difficult to further constrain ω_b from power spectrum measurements alone. In the quasi-linear to nonlinear regime at $k \sim 0.1 - 1 h \text{Mpc}^{-1}$, the power spectrum holds significant information regarding σ_8 and w , but degeneracies become an issue. Very large scales are particularly sensitive to the spectral index and ω_m , which sets the epoch of matter-radiation equality and hence the position of the peak in the power spectrum.

Next we investigate the change of the PC weight functions under the influence of varying cosmological parameters. Figure 11 shows the results for the PC weights $w_1(\theta)$ to $w_5(\theta)$ corresponding to the PCs shown in Figure 8. We show the results as a function of two of the active parameters, ω_m and n_s , while holding the remaining three parameters fixed at their midpoints. Note the very smooth behavior of the weights as a function of the parameters. The behavior of the PC weight functions can be loosely connected to the correlation functions in the following way: if the posterior mean surface for the PC weight functions looks well behaved (no steep or abrupt changes) then the correlation functions are likely away from zero. This means the surface is easy to predict at untried input settings. However, if it changes drastically, one or more of the correlation functions is near zero, and the GP will not give very accurate predictions for $w_i(\theta)$ at new input settings, as discussed above.

The sensitivity analysis is also helpful in the targeted augmentation of simulation designs. If the accuracy of the emulator is not sufficient for the problem of interest, one would like to improve it by adding additional simulations. These simulations would then involve variations of the most active parameters while keeping the other parameters more or less fixed. The augmentation of existing designs is an active field of research in statistics, and potentially important in precision cosmology applications.

3. CONCLUSIONS

The last three decades have witnessed unprecedented progress in cosmology. From order of magnitude and factor of two estimates for cosmological parameters, we now have measurements at 10% accuracy or better. These measurements have revealed one of the biggest mysteries in physics today: a dark energy leading to the acceleration of the expansion of the Universe. In order to understand the origin, nature, and dynamics of this dark energy – or to prove that the acceleration is due to a modification of gravity on the largest length scales – the accuracy of the measurements must be further improved. The next step, as defined by near-term and next-generation surveys is to obtain measurements at the 1% accuracy level. This puts considerable stress on the quality of theoretical predictions, which have to be at least as accurate. Four major probes of dark energy – baryon acoustic oscillations, weak lensing, redshift space distortions and clusters – are based on measurements of the large scale structure in the Universe. In order to obtain precise predictions for these probes, expensive, nonlinear simulations have

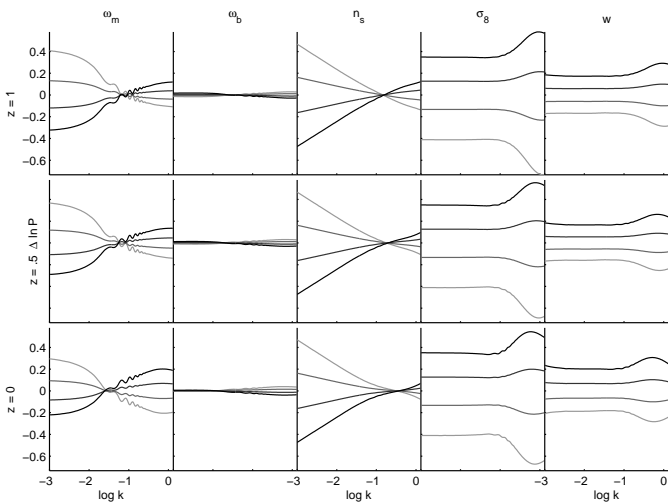


FIG. 10.— Sensitivity analysis for each of the five parameters at redshift $z = 0$, 0.5 , and 1 (bottom to top). The y-axis shows the deviation of the log of the power spectrum from the nominal spectrum where each parameter is set at its midpoint. The light to dark lines correspond to the smallest parameter setting to the largest. Due to the tight constraints on ω_b from CMB measurements, which led us to choose a rather narrow prior, ω_b variation leads to very little change in the power spectrum. Creating this plot from simulations directly would have required additional 20 simulations, costing $\sim 400,000$ CPU-hours.

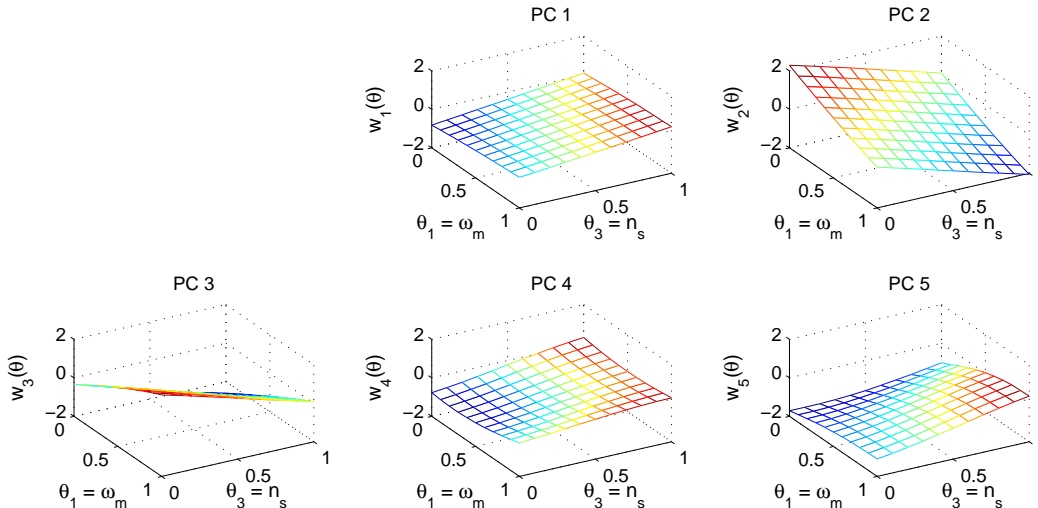


FIG. 11.— Posterior mean estimates of the principal component weight functions $w_1(\theta)$ to $w_5(\theta)$. Here the prediction points θ are over a grid of ω_m and n_s values, while the remaining parameters are held fixed at their midpoints. The cosmological parameters are displayed in the normalized $[0,1]$ space.

to be carried out and ways must be found to extract the needed information from a limited number of such simulations.

In this paper, we have demonstrated that if very accurate simulations are available, 1% accurate prediction schemes can be produced from just tens of high-accuracy simulations. The focus of this paper is the nonlinear matter fluctuation power spectrum, but the general scheme applies to any other cosmological statistic, e.g., the halo mass function, statistics of extrema, higher order functions, velocities, etc.

In Heitmann et al. (2008) we introduced a set of 38 cosmological simulations, the Coyote Universe suite, all of which satisfy the 1% error control criterion for the power spectrum up to $k \sim 1 h\text{Mpc}^{-1}$. In the current paper we demonstrate (on HALOFIT generated spectra) that from these simulations we can generate an emulator for the nonlinear power spectrum which has essentially the same accuracy as the simulations themselves. The high accuracy attained from a small number of simulation inputs is due to (i) understanding the physical variables to use as inputs to the interpolation from our detailed knowledge of cosmological perturbation theory, (ii) an interpolation method based on a sophisticated simulation design and GP modeling which has been developed and refined in the statistics community over the last decade to address problems of the nature described here, and (iii) the excellent parameter constraints from CMB measurements, which allow us to base our emulator on relatively narrow parameter priors and therefore ease the interpolation task.

This paper is the second in a series of three papers with the final goal to provide a high-precision emulator for the nonlinear power spectrum out to $k \sim 1 h\text{Mpc}^{-1}$. The first paper of the series (Heitmann et al. 2008) demonstrated that the matter power spectrum could be calculated to $\mathcal{O}(1\%)$ from well controlled N -body simulations. The current paper introduces the cosmologies underlying the Coyote Universe simulation suite, explaining and demonstrating success of the emulation technology using HALOFIT as a proxy for the simulation results. Our prediction scheme can achieve 1% accuracy from only a limited number of simulations: approximately 37 cosmological models are adequate for this purpose. The third and final paper will present results from the simulation suite discussed in this paper and will include a power spectrum emulator built around them.

This emulator will be publicly released.

Part of this research was supported by the DOE under contract W-7405-ENG-36, and by a DOE HEP Dark Energy R&D award. SH, KH, DH, and CW acknowledge support from the LDRD program at Los Alamos National Laboratory. MJW was supported in part by NASA and the DOE. We would like to thank Dragan Huterer, Lloyd Knox, Nikhil Padmanabhan, and Michael Schneider for useful discussions. K.H. is grateful to the SAMSI Summer School on the Design and Analysis of Computer Experiments for hospitality and especially thanks Jerry Sacks and Will Welch for their outstanding lectures, which guided some of the introductory section on GP modeling in this paper.

APPENDIX

OPTIMIZATION OF SPACE FILLING DESIGNS

As mentioned in Section 2.1 none of the discussed design strategies (OA, LH, OA-LH, SLH) provide a unique “best” design. For a given number of parameters, m , and the number of simulations, n , a large number of possible designs exist (e.g. for LH designs, the number is $(n!)^{m-1}$). The question is then how to choose the most suitable design for a given problem. A major requirement for the designs used in this paper is that they should have good space-filling properties. Figure A12 shows two LH designs. As explained in Section 2.1, in an LH design in every column every entry appears only once, which is clearly fulfilled for both designs shown. In the panel on the right the minimum distance between points was maximized, clearly leading to better space-filling properties. In the following we will describe two possible optimization criteria for OA-LH designs and for SLH designs which have been used in our work. We closely follow the discussion in Santner et al. (2003).

Maximin Distance Design

Our aim in optimizing the space-filling properties in our design is that no two points in the design are too close. In the example in Figure A12 we use the maximin distance optimization to spread the points out in the two dimensional plane. This optimization scheme maximizes the minimum distance between

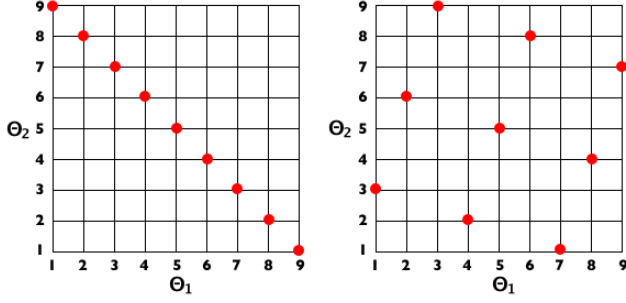


FIG. A12.— Two random LH designs. The left panel is clearly an unfortunate design, not fulfilling our requirements about space-filling. The right panel shows an LH design in which the minimum distance between points is maximized. The space-filling properties of this design are much better.

points. A more general approach is to minimize the “average” of some function of the distances between pairs of design points. As a first step, we have to define a distance measure between design points. Suppose we have an arbitrary n -point design \mathcal{D} with input settings $\{\mathbf{x}_1, \mathbf{x}_2, \dots, \mathbf{x}_n\}$ and we want to vary m parameters. The p^{th} order distance between two input settings is defined as

$$\rho_p(\mathbf{x}, \mathbf{x}') = \left[\sum_{j=1}^m |x_j - x'_j|^p \right]^{1/p}, \quad p \geq 1. \quad (\text{A1})$$

For $p = 1$ this is known as the rectangular distance, for $p = 2$ it is the Euclidean distance. Next we define the average distance criterion as follows:

$$d_{(p,\lambda)}(\mathcal{D}) = \left(\frac{2}{n(n-1)} \sum_{\mathbf{x}_i, \mathbf{x}_j} \left[\frac{m^{1/p}}{\rho_p(\mathbf{x}_i, \mathbf{x}_j)} \right]^\lambda \right)^{1/\lambda}, \quad \lambda \geq 1. \quad (\text{A2})$$

The combinatorial factor $n(n-1)/2$ is simply the number of different pairs, $(\mathbf{x}_i, \mathbf{x}_j)$, that can be drawn from the n points in the design \mathcal{D} and $m^{1/p}$ is the maximum distance between two points in $[0, 1]^m$ (where we have normalized the domain of each input variable to $[0, 1]$ as in the main paper):

$$0 < \rho_p(\mathbf{x}_i, \mathbf{x}_j) \leq m^{1/p}. \quad (\text{A3})$$

For fixed (p, λ) , an n -point design \mathcal{D}_{av} is optimal if

$$d_{(p,\lambda)}(\mathcal{D}_{av}) = \min d_{(p,\lambda)}(\mathcal{D}). \quad (\text{A4})$$

For example, if $\lambda = 1$, this condition will lead to a design which avoids “clumpiness”. The optimal average distance designs might not be optimal in projected spaces. In the main paper we mentioned that often only a few parameters are active (for example for the matter power spectrum the main active parameters are σ_8 and ω_m) and therefore it is desirable for designs to have good coverage if projected down onto two or three dimensions. Such designs can be found by computing Eq. (A2) for each relevant projection of the full design \mathcal{D} and averaging these to form a new function which is then minimized. An implementation of this approach can be found in Welch (1985). To be more concrete, let us start again with a candidate design \mathcal{D} . Now we want to consider the projection in j dimensions. This will lead to designs \mathcal{D}_{kj} which are the k -th projection onto j dimensions. Following our example in the main text, where we discussed a design with $m = 3$ parameters and we want good space-filling properties onto $j = 2$ dimensions (as shown in Figure 2), we have $k = 3$ projections. Following Eq. (A2), the average distance criterion function for the projected design \mathcal{D}_{kj} is

given by

$$d_{(p,\lambda)}(\mathcal{D}_{kj}) = \left(\frac{2}{n(n-1)} \sum_{\mathbf{x}_h^*, \mathbf{x}_i^*} \left[\frac{j^{1/p}}{\rho_p(\mathbf{x}_h^*, \mathbf{x}_i^*)} \right]^\lambda \right)^{1/\lambda} \quad (\text{A5})$$

where \mathbf{x}_i^* is the projection of \mathbf{x}_i onto \mathcal{D}_{kj} . We can now define the average projection design criterion function to be:

$$\text{av}_{(p,\lambda)}(\mathcal{D}) = \left(\frac{1}{\sum_{j \in J} C(m, j)} \sum_{j \in J} \sum_{k=1}^{C(m, j)} [d_{(p,\lambda)}(\mathcal{D}_{kj})]^\lambda \right), \quad (\text{A6})$$

with $C(m, j) = m!/[j!(m-j)!]$. An n -point design, \mathcal{D}_{avp} , is optimal with respect to the criterion given in Eq. (A6) if

$$\text{av}_{(p,\lambda)}(\mathcal{D}_{avp}) = \min \text{av}_{(p,\lambda)}(\mathcal{D}). \quad (\text{A7})$$

Now that we have defined the average projection design criterion function, including good projection properties, we can judge if a design is close to optimal. For the design used in the main part of the paper, we used two different optimization algorithms and picked the optimal design in the end by choosing the one with the better performance with respect to the distance based criterion. In the following, we will briefly outline the two algorithms. Both algorithms were used to optimize symmetric LH designs.

Simulated Annealing Algorithm for Optimized SLH Designs

The simulated annealing (SA) algorithm was introduced by Morris & Mitchell (1995) to search for optimal LH designs. We adopt the algorithm here for symmetric and non-symmetric LH designs. The basic idea is to exchange points in the design within a column, evaluate the quality of the new design by a distance criterion, and keep the new design if it is better than the previous. To be more concrete, the algorithm begins with a randomly chosen LH design for which the distance criterion is measured. Then a random column is picked and within that column two randomly picked elements are exchanged. If the design is symmetric, it is important to do the exchange in sets of pairs to keep the symmetry of the design. Suppose in a 4-row SLH design element 1 is exchanged with element i , then element 4 must be exchanged with element $5 + 1 - i$. No exchange is needed if element i is exchanged with element $n + 1 - i$ (for an excellent description of the procedure see Ye et al. 2000). If the design has an odd number of rows, the center point – which must be a design point – remains untouched. In this way, a new design \mathcal{D}_{try} is generated. The quality of the new design is measured via the distance criterion and if the design is better than the previous one it is kept. If the design is worse, it will replace \mathcal{D} with the probability $\pi = \exp\{-[\phi(\mathcal{D}_{\text{try}}) - \phi(\mathcal{D})]/t\}$ where t is a preset parameter, referred to as temperature (the form of the probability gave the algorithm its name). $\phi(\mathcal{D})$ is the criterion value for the design \mathcal{D} . This procedure works like a Markov Chain Monte Carlo, the idea being that after some time the optimization procedure will reach a local minimum close to an optimal design. The value for the temperature t influences the search area for the optimal design, the higher the value of t , the more global the search will be. Obviously, this will slow down the search, since designs which might not be very good, are kept with higher probability. In practice, the algorithm is stopped after some time and restarted from a range of random initial designs. In the end, the design with the best value for the distance criterion is kept.

A simple example for the first step in an SA algorithm is shown in Figure A13. We start with a “random” design, in this

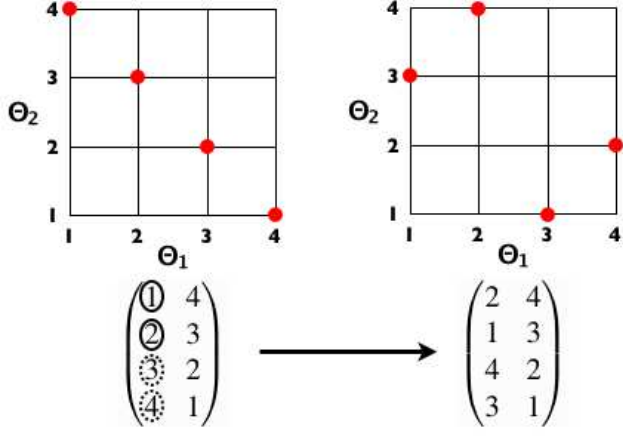


FIG. A13.— A random symmetric LH design with two parameters ($m = 2$) and four design points ($n = 4$). The first two elements that are exchanged are marked by the circle, the pair that has to be exchanged in addition to keep the symmetry is marked by dashed circles. The right panel shows an improved design after one SA step. The value for the distance criterion for the second design signals improvement, points are spread out more evenly.

case all design points are on the diagonal. Note, that this is an acceptable symmetric LH design. In this example, we have $n = 4$ design points and $m = 2$ parameters. This design is obviously not optimal, the points in the design are not evenly spread out and there are many small distances between the points close to the center of the plane. Following Eq. (A1), choosing $p = 2$ for an Euclidian distance measure and normalizing all design points to $[0, 1]^2$, we find that the maximum distance is $\sqrt{2}$ (between the two corner points), obeying Eq. (A4). The value for the distance criterion given by Eq. (A2) is easily calculated (we choose $\lambda = 1$): $d_{(2,1)}(\mathcal{D}) \simeq 2.2$. Now we try to improve the design following the scheme outlined above. We pick randomly column 1 and exchange the first two elements. To keep the symmetry, we have to also exchange element 3 and 4. The new design has a better value for the distance criterion, $d_{(2,1)}(\mathcal{D}_{\text{try}}) \simeq 1.95$, we therefore keep the design. Now we can repeat the procedure until we find an optimal design or we decide to stop the process. The first new design is shown in the right panel in Figure A13 and is clearly better than the original design.

Columnwise-pairwise Algorithm for Optimized SLH Designs

As for the SA algorithm, the columnwise-pairwise (CP) algorithm is based on columnwise-pairwise exchanges. The first major difference between the two algorithms is that the CP algorithm stops once a new design is found that is better than the previous. The second major differences is that, for each column, elements are exchanged until the best configuration for each column is found. In this regard, the CP algorithm is a more local algorithm and will most likely converge to a local optimum and rarely to a global optimum. Following Ye et al. (2000), the algorithm can be summarized as follows:

1. As in the case of an SA algorithm, start with a random SLH design.
2. Each iteration has m steps, one for each column. At the i th step, the best two simultaneous exchanges within column i are found (remember, in order to keep the symmetry, one always has to do two simultaneous exchanges). The term “best exchanges” refers again to the

quality of the global design with respect to a distance criterion. The design matrix is updated accordingly.

3. If the overall new design is better with respect to the distance criterion, repeat Step 2. Otherwise, the new design is considered to be “optimal” and the search is terminated.

As for the SA algorithm one should create several optimal designs starting from different initial designs and determine which one of the resulting designs is the best one.

GAUSSIAN PROCESS MODELING OF THE PC WEIGHT FUNCTIONS

In this appendix we discuss the full GP modeling process for the PC weights. The major differences between the discussion here and the discussion in the main text are:

- The dimensionality of the problem is increased.
- A full Bayesian treatment of the problem is performed, including full priors for correlation parameters.
- We drop the assumption that our measurements are perfect and introduce $\lambda_{\mathcal{P}}$ (see below) to account for simulation errors and errors due to the truncation in the basis functions.
- We use a slightly different correlation function.

Consider the full problem stated in the text, where θ lives in a $n_{\mathcal{P}} = 5$ dimensional space and represents a cosmology with $n_{\theta} = 5$ input parameters. We model each PC weight function $w_i(\theta)$, $i = 1, \dots, 5$ as a mean-zero GP

$$w_i(\theta) \sim GP(0, \lambda_{w_i}^{-1} R(\theta, \theta'; \rho_{w_i})), \quad (\text{B1})$$

where the symbol \sim means “distributed according to”. Here λ_{w_i} is the marginal precision of the process and the correlation function is given by:

$$R(\theta, \theta'; \rho_{w_i}) = \prod_{l=1}^{n_{\theta}} \rho_{w_i;l}^{4(\theta_l - \theta'_l)^2}. \quad (\text{B2})$$

This form is mathematically equivalent to that of Eq. (15) – set $n_{\theta} = 1$, $i = 1$, and $\rho = e^{-\theta^2/4}$. The parameter $\rho_{w_i;l}$ controls the spatial range for the l th input dimension of the process $w_i(\theta)$. Under this parametrization, $\rho_{w_i;l}$ gives the correlation between $w_i(\theta)$ and $w_i(\theta')$ when the input conditions θ and θ' are identical, except for a difference of 0.5 in the l th component. Our task is now to find λ_{w_i} and $\rho_{w_i;l}$ from the set of our simulations.

From our 37 simulations, we first define a 5-component, 37-vector w_i with $i = 1, \dots, 5$:

$$w_i^* = (w_i(\theta_1^*), \dots, w_i(\theta_{37}^*))^T. \quad (\text{B3})$$

The star indicates that we use our 37 input cosmologies here and therefore the answer for \mathcal{P} is known at that point. Assume that w^* is normal-distributed with mean zero:

$$w^* \sim N(0, \Sigma_w), \quad (\text{B4})$$

where $\Sigma_w = \text{diag}(\Sigma_{w_1}, \dots, \Sigma_{w_5})$ and $\Sigma_{w_i} \equiv \lambda_{w_i}^{-1} R(\theta^*; \rho_{w_i})$ – the 37×37 matrix obtained by applying Eq. (B2) to each pairwise combination of the 37 design points $\theta_1^*, \dots, \theta_{37}^*$. Σ_w is therefore controlled by five precision parameters λ_w and the 25 spatial correlation parameters held in ρ_w . Next we have to specify priors for each λ_{w_i} and for the $\rho_{w_i;l}$. Following Habib et al.

TABLE B4
DEFINITIONS AND EXPLANATIONS OF VARIABLES USED IN THIS SECTION

| Variable number/value | Explanation |
|--|--|
| $\Phi = [\phi_1; \dots; \phi_5]$ | PC basis matrix, consisting of orthogonal basis vectors |
| $\mathcal{P} = \ln[\Delta^2(k, z)/(2\pi k^3/2)]$ | Rescaled power spectrum |
| $n_{\mathcal{P}}=5$ | Number of principal components |
| $n_{\theta} = 5$ | Number of cosmological parameters |
| $\theta = \omega_m, \omega_b, n_s, w, \sigma_8$ | Cosmological parameters |
| $w_i(\theta)$ | GP model of PC weights for i^{th} basis function |
| w_i^* | GP model of PC weights for i^{th} basis function at the design settings $\theta_1^*, \dots, \theta_m^*$ |
| w^* | GP model of all PC weights at design inputs: $\text{vec}(w_1^*, \dots, w_{n_{\mathcal{P}}}^*)$ |
| \hat{w} | PC weights obtained from projecting simulation output onto bases; contains numerical error |
| $m = 37$ | Number of cosmological models |
| λ_{w_i} | Marginal precision of the GP process for the i^{th} PC |
| ρ_w | Correlation functions |
| $\lambda_{\mathcal{P}}$ | Precision describing simulation and truncation error |
| $n_{kz} = 20000$ | Number of points for each power spectrum (200 k -values at 100 redshifts) |
| $a_{\rho_w} = 1, b_{\rho_w} = 0.1$ | Prior parameters in the β -distribution for the $\rho_{w;il}$'s |
| $a_w = 5, b_w = 5$ | Prior parameters in the Γ -distribution for the λ_{w_i} 's |

(2007), we choose $\Gamma(a_w, b_w)$ distributions for the priors for λ_{w_i} and $\beta(a_{\rho_w}, b_{\rho_w})$ priors for the $\rho_{w;il}$:

$$\pi(\lambda_{w_i}) = \frac{1}{\Gamma(a_w)} b_w (b_w \lambda_{w_i})^{a_w-1} e^{-b_w \lambda_{w_i}}, \quad i = 1, \dots, 5, \quad (\text{B5})$$

$$\pi(\rho_{w;il}) = \frac{\Gamma(a_{\rho_w} + b_{\rho_w})}{\Gamma(a_{\rho_w})\Gamma(b_{\rho_w})} \rho_{w;il}^{a_{\rho_w}-1} \times (1 - \rho_{w;il})^{b_{\rho_w}-1} \quad i = 1, \dots, 5, \quad l = 1, \dots, 5 \quad (\text{B6})$$

with $a_w = b_w = 5$, $a_{\rho_w} = 1$, and $b_{\rho_w} = 0.1$. The choices for a_w and b_w lead to a prior for λ_{w_i} of mean 1 and a prior standard deviation of 0.45 (The mean of a Γ distribution is given by a/b and the standard deviation by $\sqrt{a/b^2}$). The choice of unit mean is consistent with the standardization of the GP for the w_i .

The choices for a_{ρ_w} and b_{ρ_w} lead to a substantial prior mass near 1 [The mean of a β distribution is given by $a/(a+b)$ and the standard deviation by $\sqrt{ab/((a+b)^2(a+b+1))}$.] In general, the selection of these parameters depends on how many of the n_{θ} inputs are expected to be active.

Now we return to the *actual* information that we have, and from which we want to derive the weights w_i : the simulation outputs for the power spectra \mathcal{P}^* for the 37 cosmologies. We arrange these outputs in an $n_{kz}m$ vector

$$\mathcal{P}^* = \text{vec}([\mathcal{P}(\theta_1^*); \dots; \mathcal{P}(\theta_{37}^*)]). \quad (\text{B7})$$

The simulation outputs have two sources of error: the error intrinsic to the simulation (e.g., realization scatter, numerical error) and the error due to the truncation in basis functions used to model $\mathcal{P}(k; \theta)$ via Eq. (11). We encapsulate the precision of the error in $\lambda_{\mathcal{P}}$ and we assume that the error ϵ itself in Eq. (11) is independent and identically normal distributed. We are now in a position to formulate the likelihood for \mathcal{P}^* :

$$p(\mathcal{P}^* | w^*, \lambda_{\mathcal{P}}) \propto \lambda_{\mathcal{P}}^{mn_{kz}/2} \exp\left\{-\frac{1}{2} \lambda_{\mathcal{P}} (\mathcal{P}^* - \Phi w^*)^T (\mathcal{P}^* - \Phi w^*)\right\}, \quad (\text{B8})$$

where Φ is a matrix composed from the ϕ_i basis vectors which we use to model the power spectra (see Eq. (11)). As for λ_w , we specify the priors by a $\Gamma(a_p, b_p)$ distribution. We expect the data to be very informative about $\lambda_{\mathcal{P}}$ and therefore choose

the prior to be very broad with $a_p = 1$ and $b_p = 0.0001$. This prior allows for large values of $\lambda_{\mathcal{P}}$ which force the GP model to nearly interpolate the simulation output. This will happen when the PC representation of the output is very good.

This result is only an intermediate step, as our goal is to find the likelihood for the w_i not for \mathcal{P} itself. Fortunately, we can factorize Eq. (B8) to extract the likelihood for the weights easily. To do this we define \hat{w} as

$$\hat{w} = (\Phi^T \Phi)^{-1} \Phi^T \mathcal{P}^*. \quad (\text{B9})$$

Note that \hat{w} encapsulates the error due to the truncation of the basis functions in modeling \mathcal{P}^* . With this definition, it is easy to show that Eq. (B8) can be written as

$$p(\mathcal{P}^* | w^*, \lambda_{\mathcal{P}}) \propto \lambda_{\mathcal{P}}^{mn_{\mathcal{P}}/2} \exp\left\{-\frac{1}{2} \lambda_{\mathcal{P}} (w^* - \hat{w})^T (\Phi^T \Phi) (w^* - \hat{w})\right\} \times \lambda_{\mathcal{P}}^{m(n_{kz}-n_{\mathcal{P}})/2} \times \exp\left\{-\frac{1}{2} \lambda_{\mathcal{P}} \mathcal{P}^{*T} (I - \Phi(\Phi^T \Phi)^{-1} \Phi^T) \mathcal{P}^*\right\}, \quad (\text{B10})$$

with $m = 37$, $n_{\mathcal{P}} = 5$, and n_{kz} denoting the (k, z) support for each power spectrum is measured. Note that in the first line of Eq. (B10), \hat{w} is completely separated from the rest of the likelihood expression. We can use this factorization to represent the likelihood in a dimension-reduced form:

$$p(\hat{w} | w^*, \lambda_{\mathcal{P}}) \propto \lambda_{\mathcal{P}}^{mn_{\mathcal{P}}/2} \exp\left\{-\frac{1}{2} \lambda_{\mathcal{P}} (w^* - \hat{w})^T (\Phi^T \Phi) (w^* - \hat{w})\right\}, \quad (\text{B11})$$

where the remaining terms from Eq. (B10) are absorbed in a re-defined Gamma distribution prior for $\lambda_{\mathcal{P}}$, $\Gamma(a'_p, b'_p)$ with

$$a'_p = a_p + \frac{m(n_{kz} - n_{\mathcal{P}})}{2}, \quad (\text{B12})$$

$$b'_p = b_p + \frac{1}{2} \mathcal{P}^T (I - \Phi(\Phi^T \Phi)^{-1} \Phi^T) \mathcal{P}. \quad (\text{B13})$$

It is useful to recap what has been done so far: We began with the normal likelihood for \mathcal{P} with the Gamma distribution prior for $\lambda_{\mathcal{P}}$:

$$\mathcal{P}^* | w^*, \lambda_{\mathcal{P}} \sim N(\Phi w^*, \lambda_{\mathcal{P}}^{-1} I_{n_{kz}}), \quad \lambda_{\mathcal{P}} \sim \Gamma(a_p, b_p). \quad (\text{B14})$$

Due to the relation

$$p(\mathcal{P}^*|w^*, \lambda_{\mathcal{P}}) \times \pi(\lambda_{\mathcal{P}}; a_{\mathcal{P}}, b_{\mathcal{P}}) \propto p(\hat{w}|w, \lambda_{\mathcal{P}}) \quad (\text{B15}) \\ \times \pi(\lambda_{\mathcal{P}}; a'_{\mathcal{P}}, b'_{\mathcal{P}}),$$

we can derive the likelihood for \hat{w} :

$$\hat{w}|w^*, \lambda_{\mathcal{P}} \sim N(w^*, (\lambda_{\mathcal{P}} \Phi^T \Phi)^{-1}), \quad \lambda_{\mathcal{P}} \sim \Gamma(a'_{\mathcal{P}}, b'_{\mathcal{P}}). \quad (\text{B16})$$

Next, w^* is integrated out, leading to the posterior distribution

$$\pi(\lambda_{\mathcal{P}}, \lambda_w, \rho_w | \hat{w}) \propto \quad (\text{B17})$$

$$\left| (\lambda_{\mathcal{P}} \Phi^T \Phi)^{-1} + \Sigma_w \right|^{-\frac{1}{2}} \\ \times \exp\left\{-\frac{1}{2} \hat{w}^T \left((\lambda_{\mathcal{P}} \Phi^T \Phi)^{-1} + \Sigma_w \right)^{-1} \hat{w}\right\} \quad (\text{B18})$$

$$\times \lambda_{\mathcal{P}}^{a'_{\mathcal{P}}-1} e^{-b'_{\mathcal{P}} \lambda_{\mathcal{P}}} \prod_{i=1}^{n_{\mathcal{P}}} \lambda_{w_i}^{a_w-1} e^{-b_w \lambda_{w_i}} \prod_{i=1}^{n_{\mathcal{P}}} \prod_{j=1}^{n_{\theta}} (1 - \rho_{w_i;j})^{b_{\rho}-1}.$$

As detailed in Habib et al. (2007) this posterior distribution is a milepost on the way to creating the emulator for the power spectrum. It can be explored via MCMC and contains much useful information about the parametric dependence of the power spectrum, as derived from the numerical simulation results at the finite number of design points.

Next, we briefly discuss the behavior of the correlation function, ρ_w , under the influence of different cosmological parameters. The results for the ρ_w are shown in Figure B14 in the form of boxplots. Boxplots are commonly used in statistical analyses – they offer a convenient way of showing the distribution of data using just five numbers (see the caption of Figure B14).

With our definitions (see also Habib et al. 2007), an input l is inactive for PC i if $\rho_{w;il} = 1$. Inactive here means that the parameter does not change the actual shape of the power spectrum. If $\rho_{w;il}$ is very close to one it can still have strong linear effects. In our case, the box values suggest that the coefficients of the first four PCs are smooth functions of all parameters. This implies that it will be easy for the GP model to predict the power spectrum at untried settings. If any box value is close to zero, it indicates there is no smooth functional connection between the parameters and coefficient values. In our case, σ_8 is the first parameter for which ρ_w is very close to zero for the coefficient of the fifth principal component, which is the last one we include in our model. This will have only a minor impact on smoothness of the overall input-output relationships as this component is negligible. Figure B14 also shows that ω_m and σ_8

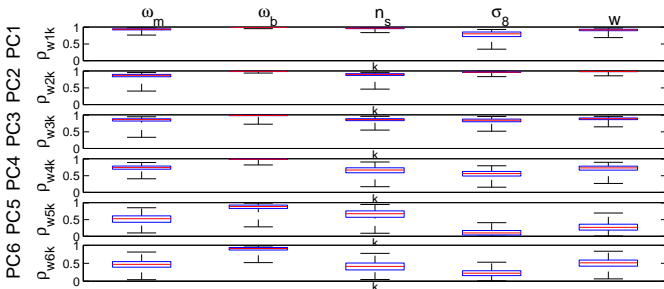


FIG. B14.— Boxplots of posterior samples for each $\rho_{w;il}$ for the nonlinear matter power spectrum. The blue box itself contains 50% of the data, the lower edge indicating the 25th percentile and the upper edge, the 75th percentile. The red (center) line denotes the median. If the red line is not at the center of the box, the data is skewed. The black lines (or whiskers) extend out to the full range of the data. With our parametrization, a box value close to 1 indicates that the parameter is inactive, i.e., the PC is not changing much under the variation of that parameter.

are the most active parameters influencing the power spectrum, as expected on physical grounds. The equation of state parameter w is also active, due to the fact that the Hubble parameter and Ω_m are changing with w . These observations are in good agreement with the sensitivity analysis of the power spectrum itself.

The last step for building the complete emulator is to draw from the posterior distribution (B17) at any given θ . We consider the joint distribution of \hat{w} and a predicted weight w_e at a new input parameter setting θ_e :

$$\begin{pmatrix} \hat{w} \\ w_e \end{pmatrix} \sim N\left(0, \left[\begin{pmatrix} (\lambda_{\mathcal{P}} \Phi^T \Phi)^{-1} & 0 \\ 0 & 0 \end{pmatrix} + \Sigma_{w,w_e}(\lambda_w, \rho_w) \right]\right) \quad (\text{B19})$$

where Σ_{w,w_e} is obtained by applying the prior covariance rule to the augmented input settings that include the original design and the new input setting (θ_e). We find

$$w_e | \hat{w} \sim N(V_{21} V_{11}^{-1} \hat{w}, V_{22} - V_{21} V_{11}^{-1} V_{12}), \quad (\text{B20})$$

where

$$V = \begin{pmatrix} V_{11} & V_{12} \\ V_{21} & V_{22} \end{pmatrix} \\ = \left[\begin{pmatrix} (\lambda_{\mathcal{P}} \Phi^T \Phi)^{-1} & 0 \\ 0 & 0 \end{pmatrix} + \Sigma_{w,w_e}(\lambda_w, \rho_w) \right] \quad (\text{B21})$$

is a function of the parameters produced by the MCMC output. Hence for each posterior realization of $\lambda_{\mathcal{P}}, \lambda_w, \rho_w$, a realization of w can be produced and the emulator is completed.

REFERENCES

- Auld, T., Bridges, M., Hobson, M.P. & Gull, S.F. 2007, MNRAS, 376, L11
Auld, T., Bridges, M., & Hobson, M.P. 2008, MNRAS, 387, 1575
Brandbyge, J., Hannestad, S., Haugboelle, T. & Thomsen, B. 2008, JCAP, 0808, 020
Bunn, E. & White, M. 1997, ApJ, 480, 6
Carlson J.W., White, M., & Padmanabhan, 2009, arXiv:0905.0479
Crocce, M. & Scoccimarro, R. 2006, Phys. Rev. D, 73, 063520
Curran C., Mitchell T., Morris, M., & D. Ylvisaker 1991, J. Am. Stat. Assn. 86, 953
Evrard, A.E. et al. 2008, ApJ, 672, 122
Fendt, W. & Wandelt, B. 2007, ApJ, 654, 2
Fendt, W. & Wandelt, B. 2007, arXiv:0712.0194
Francis, M., Lewis, G., & Linder, E. 2007, MNRAS, 380, 1079
Guillet T., Teyssier R., Colombi S., 2009, submitted to A&A [arXiv:0905.2615]
Habib, S., Heitmann, K., Higdon, D., Nakhleh, C., & Williams, B. 2007, Phys. Rev. D, 76, 083503
Hamilton, A.J.S., Kumar, P., Lu, E., Matthews, A. 1991, ApJ, 374, L1
Hedayat, A.S., Sloane, N.J.A., & Stufken, J. 1999, Orthogonal Arrays: Theory and Applications, Springer, New York
Heitmann, K., Higdon, D., Nakhleh, C., & Habib, S. 2006, ApJ 646, L1
Heitmann, K., White, M., Wagner, C., Habib, S., & Higdon, D., ApJ (submitted), arXiv:0812.1052
Higdon D., Gattiker J., & B. Williams 2008, J. Am. Stat. Assn. 103, 570
Hu, W. & White, M. 1997, ApJ, 479, 568
Hu, W. & Sugiyama, N. 1995, ApJ, 444, 489
Huterer, D. & Takada, M. 2003, Astrop. Physics, 23, 369
Jimenez, R., Verde, L., Peiris, H., & Kosowsky, A. 2004, Phys. Rev. D, 70, 23005
Jing, Y.P., Zhang, P., Lin W.P., Gao L., & Springel, V. 2006, ApJ, 640, L119
Kaplinghat, M., Knox, L., & Skordis, C. 2002, ApJ, 578, 665
Kilbinger, M. et al. 2009, A&A, 497, 677
Komatsu, E. et al. 2009, ApJS, 180, 330
Kowalski, M. et al. 2008, ApJ, 686, 749
Leary, S., Bhaskar, A., & Keane, A. 2003, Journal of Appl. Stat., 5, 585
Lewis, A. & Bridle, S. 2002, Phys. Rev. D, 66, 103511
Li, W. & Ye, K.Q. 2000, Journal of Statistical Planning and Inference, 90, 145
Linder, E. & White M. 2005, Phys. Rev. D72, 061304
Matsubara, T. 2008, Phys. Rev. D, 77, 063530
McKay, M., Beckman, R., & Conover, W., 1979, Technometrics, 21, 239
Meiksin, A. & White, M., 1999, MNRAS, 308, 1179
Morris, M.D. & Mitchell, T.J. 1995, Journal of Stat. Planning and Inference, 43, 381

- Padmanabhan N., White M., 2009, Phys. Rev. D, in press [arXiv:0906.1198]
Peacock, J.A. & Dodds, S.J. 1994, MNRAS, 267, 1020
Peacock, J.A. & Dodds, S.J. 1996, MNRAS, 280, L19
Perlmutter, P. et al. 1999, ApJ, 517, 565
Pietroni, M. 2008, JCAP, 10, 036
Rasmussen, C.E. & Williams, K.I. 2006, Gaussian Processes for Machine Learning, MIT Press, www.GaussianProcess.org/gpml
Riess A.G et al. 1998, AJ, 116, 1009
Rudd, D., Zentner, A., & Kravtsov, A. 2008, ApJ, 672, 19
Sacks, J., Welch, W.J., & Mitchell, T.J. 1989, Stat. Sci. 4, 409
Sacks, J., Schiller, S.B., & Welch, W.J. 1989, Technometrics, 34, 15
Santner, T.J., Williams, B.J., & Notz, W.I. 2003, The Design and Analysis of Computer Experiments, Springer, New York
Shewry, M. & Wynn, H. 1987, J. of Appl. Stat., 14, 2, 165
Schneider, M., Knox, L., Habib, S., Heitmann, K., Higdon, D., & Nakhleh, C., Phys. Rev. D, 78, 063529 (2008)
Smith, R.E., Peacock, J.A., Jenkins, A., White, S.D.M., Frenk, C.S., Pearce, F.R., Thomas, P.A., Efstathiou, G., & Couchman, H.M.P. 2003, MNRAS, 342, 1311
Tang, B. 1993, Am. Stat. Assoc., 88, 1392
Tegmark, M. & Zaldarriaga M. 2000, ApJ 544, 30
Tegmark, M. et al. 2006, Phys. Rev. D, 74, 123507
Vikhlinin, A. et al. 2009, ApJ, 692, 1060
Voevodkin, A. & Vikhlinin, A. 2004, ApJ, 601, 610
Welch, W.J. 1985, The American Statistician, 39, 146
White M., Vale C. 2004, Astroparticle Physics, 22, 19
White M., 2004, Astropart. Phys., 22, 211
White M., 2006, New Astronomy Reviews, 50
Ye, K.Q 1998, Journal of the Am. Stat. Assoc., 93, 1430
Ye, K.Q, Li, W., & Sudjianto, A. 2000, Journal of Stat. Planning and Interference, 90, 145
Zhan, H. & Knox, L. 2004, Astrophys. J., 616, L75